

University of Alabama in Huntsville

**LOUIS**

---

Theses

UAH Electronic Theses and Dissertations

---

2018

## **Solid rocket motor static fire test stand optimization : load cell effects and other uncertainties**

Charles W. Freeman II

Follow this and additional works at: <https://louis.uah.edu/uah-theses>

---

### **Recommended Citation**

Freeman, Charles W. II, "Solid rocket motor static fire test stand optimization : load cell effects and other uncertainties" (2018). *Theses*. 263.  
<https://louis.uah.edu/uah-theses/263>

This Thesis is brought to you for free and open access by the UAH Electronic Theses and Dissertations at LOUIS. It has been accepted for inclusion in Theses by an authorized administrator of LOUIS.

**SOLID ROCKET MOTOR STATIC FIRE TEST STAND OPTIMIZATION:  
LOAD CELL EFFECTS AND OTHER UNCERTAINTIES**

**by**

**CHARLES W. FREEMAN II**

**A THESIS**

**Submitted in partial fulfillment of the requirements  
for the degree of Master of Science in Engineering  
in  
The Department of Mechanical and Aerospace Engineering  
to  
The School of Graduate Studies  
of  
The University of Alabama in Huntsville**

**HUNTSVILLE, ALABAMA**

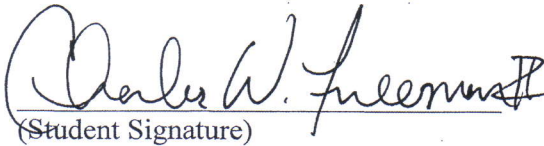
**2018**

Copyright by  
Charles W. Freeman II  
All Rights Reserved  
2018

Reproduction or translation of any part of this work beyond that permitted by Section 107 or Section 108 of the 1976 United States Copyright Act without the written expressed permission of the copyright owner is unlawful and strictly prohibited. Requests for permission or further information should be addressed to the author at

1216 County Road 463  
Cullman, AL 35057

In presenting this thesis in partial fulfillment of the requirements for a Master of Science in Mechanical and Aerospace Engineering degree from The University of Alabama in Huntsville, I agree that the Library of this University shall make it freely available for inspection. I further agree that permission for extensive copying for scholarly purposes may be granted by my advisor or, in his/her absence, by the Chair of the Department or the Dean of the School of Graduate Studies. It is also understood that due recognition shall be given to me and to The University of Alabama in Huntsville in any scholarly use which may be made of any material in this thesis.

  
(Student Signature)

14-Aug-2018  
(Date)

## THESIS APPROVAL FORM

Submitted by Charles W. Freeman II in partial fulfillment of the requirements for the degree of Master of Science in Mechanical and Aerospace Engineering and accepted on behalf of the Faculty of the School of Graduate Studies by the thesis committee.

We, the undersigned members of the Graduate Faculty of The University of Alabama in Huntsville, certify that we have advised and/or supervised the candidate on the work described in this thesis. We further certify that we have reviewed the thesis manuscript and approve it in partial fulfillment of the requirements for the degree of Master of Science in Mechanical and Aerospace Engineering.

Robert W. Fredrick 8/13/18  
(Date)

Committee Chair

Farhad Far

Paul C. Cusick

D. Kelly Halligan

Department Chair

Angela Gratz

College Dean

JBC

Graduate Dean

## ABSTRACT

The School of Graduate Studies  
The University of Alabama in Huntsville

Degree Master of Science in Engineering College/Dept. Engineering/Mechanical and  
Aerospace Engineering

Name of Candidate Charles W. Freeman II

Title Solid Rocket Motor Static Fire Test Stand Optimization: Load Cell Effects and  
Other Uncertainties

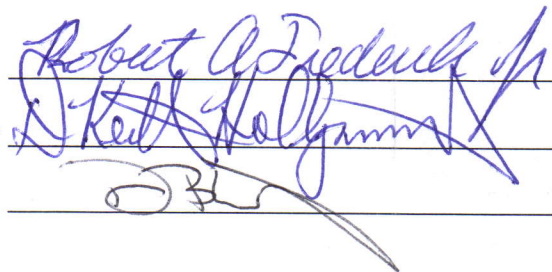
US military legacy missile systems must be periodically tested to ensure they will perform as designed during training and in times of armed conflict. The objective of this work was to assess the overall thrust measurement uncertainty of a tactical-sized solid rocket motor static thrust stand. Motor alignment, load cell / test stand dynamics, signal conditioning, data acquisition, and calibration procedures were examined as potential sources of uncertainty. The uncertainty analysis revealed that a 5,000 *lbf* thrust measurement can be made to within  $\pm 0.26\%$  of full scale with 95% confidence. The load cell / test stand / motor structural resonance was the dominate source of thrust data distortion. Increasing load cell stiffness, increased the resonant response frequency out of the analysis band for the system investigated. Low hysteresis during in-situ load cell calibrations was determined to be an excellent measure of motor / test stand alignment. A properly selected / designed load cell was shown to eliminate most requirements to digitally manipulate or post-process thrust data, e.g., filtering or data averaging, and prevent the unintentional suppression of any real-world physical phenomena.

Abstract Approval:

Committee Chair

Department Chair

Graduate Dean



## ACKNOWLEDGMENTS

The work presented in this thesis would not have been possible without the guidance and assistance of many special people. Although each person may not be specifically named here, I would like to express a heartfelt thank you to everyone who has supported me and cheered me on during this very fulfilling work. First, I would like to thank my advisor and committee chairman, Dr. Robert A. Frederick Jr., and my committee members, Dr. Jason Cassibry and Dr. Farbod Fahimi, for their assistance in helping me define this topic of the research and for their guidance throughout all the stages of this journey. Second, I would like to thank my co-workers for their contributions to this work. Without their expertise and willingness to assist, this work would have not been possible. Finally, I would like to thank all the members of the United States Military. This work was performed with the ultimate goal of supplying each soldier with best and most reliable equipment possible as they risk their lives in service to, and in protection of, the American people, our liberty, and our freedoms.

I would like to thank my family, who are my inspiration in life and in all that I hope to accomplish, they are my heroes and the true loves of my life. I spent many hours away from them studying and working and I never received even the slightest complaint. Without their support, encouragement, and love I would have never be able to begin or complete this or any work.

Most importantly I give all credit and thanks to my Lord God, who through all things are possible. I thank Him for the support system has seen fit to supply to me, for any ability or talent I may possess, and for the hope of everlasting salvation through His Son, Jesus Christ.

## TABLE OF CONTENTS

	Page
List of Figures.....	viii
List of Tables.....	x
List of Symbols.....	xi
Chapter	
I. INTRODUCTION.....	1
A. Background and Motivation.....	1
B. L-Block Static Fire Test Methodology.....	3
C. Load Cells and Measuring Thrust.....	7
D. Rocket Thrust Measurement Literature Review.....	10
II. THE PRINCIPLE OF UNCERTAINTY .....	14
A. A Précis on Uncertainty.....	14
B. The Utility of Uncertainty.....	16
C. Rocket Thrust Measurement Uncertainty Literature Review.....	27
III. THRUST MEASUREMENT STUDY.....	27
A. Dynamic Effects .....	27
B. Motor Alignment.....	45
C. Signal Condition System (SCS).....	53
D. Data Acquisition System (DAS).....	57
E. Load Cell Calibration .....	58
F. Overall Measurement Uncertainty.....	60
IV. DISCUSSION AND CONCLUSIONS.....	61



APPENDIX A: SCS Factor Acceptance Testing (FAT).....	64
APPENDIX B: Example Calculations.....	69
REFERENCES.....	74

## LIST OF FIGURES

Figure	Page
1.1 Solid Rocket Motor Firing from a Mobile L-block.....	3
1.2 Solid Rocket Motor Firing from a Fixed L-block.....	4
1.3 Ring/Roller Bearing Arrangement used for Centering and Leveling.....	6
1.4 Typical Static Motor Firing .....	6
1.5 Typical Strain Gauge Based, Canister Type Load Cell.....	8
1.6 Typical Strain Gauge.....	9
1.7 Typical Thrust Data Plot.....	9
2.1 Accuracy versus Precision.....	15
2.2 Error Relationship between a True Value and its Measured Value .....	18
3.1 Preload-Rig for a Tactical Size Rocket Motor.....	28
3.2 Static Firing Configuration for an Inert, Tactical Size Rocket Motor.....	31
3.3 Modal Accelerometer Placement and Example Impact Locations.....	32
3.4 Modal Analysis Results of the Tactical Size Rocket Motor Setup.....	33
3.5 Characteristic Ringing in a Generic Thrust Plot.....	36
3.6 Theoretical Thrust Adapter 1, Dominate Mode 3.....	39
3.7 Theoretical Thrust Adapter 2, Dominate Mode 3.....	39
3.8 Legacy Thrust Adapter, Dominate Mode 3.....	40
3.9 Load Cell Comparison.....	41
3.10 Raw Thrust Data Acquired from a Legacy Load Cell.....	42
3.11 Raw Thrust Data Acquired from the New Design.....	43
3.12 Thrust Curve Actual Comparison, Legacy Load Cell versus the New Design....	44

3.13	Setup to Determine the TBDG Measurement Uncertainty.....	46
3.14	TBDG Mock Motor Measurement Setup.....	50
3.15	Load Cell Loading Setup.....	52
3.16	Measurement Path Hysteresis.....	52
3.17	Simplified Bridge Type Conditioner Channel Block Diagram.....	54
3.18	Simplified Schematic of Signal Path through the DAS.....	57
3.19	5,000 lbf, Primary Deadweight Force Calibration Machine.....	59
A.1	Gain Error Test Method to determine Overall SCS Uncertainty.....	66
A.2	OEM Published DVM AC Characteristics.....	67
A.3	OEM Published DVM DC Characteristics.....	68

## LIST OF TABLES

Table	Page
3.1     Calculated Load Cell Resonance Frequencies for an Approximated Tactical Size Rocket Motor Static Fire Test.....	35
3.2     Estimated Load Cell Ringing Frequency from an Actual Tactical Size Rocket Motor Static Fire Test.....	37
3.3     Thrust Adapter Weight and Frequency for the First Four Mode Shapes.....	38
3.4     Comparison of Load Cell Design Parameters.....	42
3.5     TBDG Measurement Uncertainty Calculation Results.....	48
3.6     Relative Mock Motor Height Measurements .....	50
3.7     Bridge Conditioner Uncertainty Parameters .....	55
3.8     SCS Uncertainty Analysis.....	56
3.9     DAS Uncertainty Analysis.....	58
3.10    Load Cell Calibration Uncertainty.....	60
3.11    Overall Thrust Measurement Uncertainty.....	60

## LIST OF SYMBOLS

Symbol	Definition
$\Phi$	Cumulative Distribution Function
$\Phi^{-1}$	Inverse Cumulative Distribution Function
%	Percent
°	Degrees
$\Delta$	Delta
AC	Alternating Current
ADC	Analog-to-Digital Converter
Amp	Amplifier
$A_{OL\_DC}$	Open-Loop gain at DC
AUR	All-Up-Round
ASP	Ammunition Supply Point
ASTM	American Society for Testing and Materials
B	Expanded Systematic Error
$\beta$	Systematic Standard Error or Feed Back
cal	Calibration
$C_{Bik}$	Correlation Coefficient for Systematic Errors
CDF	Cumulative Distribution Function
$C_{Eik}$	Correlation Coefficient for Random Errors
$C_L$	Confidence Level
$\frac{d}{dt}$	Change with respect to Time
$\delta$	Partial Derivative

$d$	Local Air Density
$D$	Density of the Calibration Weight
DAS	Data Acquisition System
dB	Decibels
DC	Direct Current
DOF	Degrees of Freedom
DOI	Digital Object Identifier
DRE	Data Reduction Equation
$d_{\text{spring}}$	Spring Deflection
DVM	Digital Volt Meter
$\text{Err}_t$	Total Error
$\text{Err}_H$	Height Measurement Error
$\varepsilon$	Random Standard Error
$e$	Natural Logarithm Base
$E$	Expanded Random Error
e.g.	Exempli Gratia, Latin for “for example”
Exc	Excitation
$f_0$	Dominant Pole of an Operational Amplifier
$f$	Test Frequency
$f_{\text{approx}}$	Approximated Frequency
$f_n$	Natural Resonance Frequency
$f_{\text{peak}}$	Peak Frequency
FAT	Factory Acceptance Testing

$F$	Measured Thrust
$F_{\max}$	Maximum Thrust
FS	Full Scale
$FS_{\text{in}}$	Full Scale In
$FS_{\text{out}}$	Full Scale Out
$F_{\text{spring}}$	Force Exerted on a Spring
fwd	Forward
FWG	Function/Waveform Generator
$f(x)$	Frequency of a Measurement within a Normal Distribution
$g$	Gravitational Constant
$H_{\text{act}}$	Actual Height
$H_{\text{meas}}$	Measured Height
Hz	Hertz
ICDF	Inverse Cumulative Distribution Function
i.e.	id est, Latin for “in other words”
in	Inch(es)
K	Spring Constant
lb(s)	Pound(s)
lbf	Pounds Force
LP	Low Pass
LSA	Large Sample Assumption
m	Mass
$m_e$	Mass of Measurement Element

$m_l$	Mass of Load
$m_p$	Mass of Propellant
$M_{lim}$	Measure limits
$M_v$	Measured Value
$n$	Number of ADC Bits
$N$	Number of Samples
NGS	National Geodetic Survey
NIST	National Institute of Standards and Technology
NOAA	National Oceanic and Atmospheric Administration
$\sigma$	Standard Deviation
OEM	Original Equipment Manufacturer
OL	Open-Loop
$P$	Parameter
$\pi$	Constant, $\sim 3.142$
ppm	Parts Per Million
Prog	Programmable
$r$	Result
Reg	Regulator
RDT&E	Research, Development, Test, and Evaluation
RMS	Root Mean Square
RTC	Redstone Test Center
RTI	Referred-to-Input
RTO	Referred-to-Output



SCS	Signal Conditioning System
Sensor <sub>sens</sub>	Sensor Sensitivity
SRP	Stockpile Reliability Program
$s_x$	Standard Deviation
$s_{\bar{x}}$	Mean Standard Deviation
$T_v$	True Real-World Value
$t$	Student's $t$ -Distribution Value
$\tau$	Population set range
TBDG	Twin Beam Dial Gauge
TUR	Test Uncertainty Ratio
$u$	Standard Uncertainty
$u_r$	Standard Uncertainty of Result
$u_{are}$	Uncertainty of Analog Reading Error
$u_{ee}$	Uncertainty of Evaluator Error
$u_{rme}$	Uncertainty of Repetitive Measurement Error
$u_{\overline{rme}}$	Uncertainty of Average Repetitive Measurement Error
$u_{r, meas}$	Resultant Measurement Uncertainty
$U$	Expanded Uncertainty
$U_{adc, 95\%}$	Expanded Uncertainty of Analog-to-Digital Converter
$U_r$	Expanded Uncertainty of Result
$U_{r, 25^\circ C}$	Expanded Uncertainty of Result at 25°C
$U_{r, 40^\circ C}$	Expanded Uncertainty of Result at 40°C
$U_{r, tol}$	Expanded Uncertainty of Measurement Tolerance

$\mu$	Average of a Normal Distribution
US	United States
$\nu$	Degrees of Freedom
$\nu_{\text{est}}$	Estimated Degrees of Freedom
V	Volts
$V_{\text{in}}$	Input Voltage
$V_{\text{fb}}$	Feedback Voltage
$V_{\text{max}}$	Maximum Voltage
$V_{\text{out}}$	Output Voltage
w/	with
x	Sample in a Population
X	Sample Set
$\bar{X}$	Sample Set Average
$\zeta$	Damping Ratio

# **CHAPTER I**

## **INTRODUCTION**

### **A. Background and Motivation**

The United States (US) armed forces have been on a war footing and engaged in conflicts spanning the globe for the last several decades. Due to the lack of recent design and construction of new US tactical weapon systems and US government budget constraints; the continued use of legacy weapon systems has become a major requirement and is of paramount concern. Some of these legacy systems, and their variants, are approaching 40 years of service life. In an effort to track the health of these systems and determine their continued viability, yearly Stockpile Reliability Program (SRP) testing, among other metrics, is performed on randomly sampled lots stored in various Ammunition Supply Point (ASP) locations from all over the world. These system samples are either functioned as designed in their All-Up-Round (AUR) configurations or they are disassembled into their individual components, tested, and evaluated based on individual Original Equipment Manufacturers (OEM) specifications. These results are then compared and contrasted with original performance criteria and previous year SRP testing to determine degradation trends, if they exist. As a result, SRP testing can be seen as a tool used to identify potential or worsening problems with stored weapon systems prior to placing these systems in the hands of the US warfighter. This helps ensure the US warfighter is supplied with the most reliable weapon systems / components and that these systems / components will function as designed when called upon during training or during times of armed conflict.

In light of the importance this type of testing commands, several critical questions arise; how well are these tests being performed, how ‘good’ are the measured metrics ascertained by these tests, what certainty and confidence can be assigned to these metrics, and how do these metrics play into the socioeconomic, political, and decision making processes of fielding these systems. To find resolution to these and other questions it is incumbent upon evaluators to ensure testing is being performed as accurately and precisely as possible. To achieve this goal the evaluators must have solid insight and knowledge of the system under test as well as an intimate understanding of the test equipment, from end-to-end, being employed during test events. On the surface this may seem obvious or even elementary but there are some areas (e.g., longstanding procedures and offsite calibrations) which are assumed to be correct with indifference and without even a cursory query of validity. Almost by default, and without even the slightest reservation, these types of assumptions are almost universally taken for granted and forgotten. Yet, they become the bedrock on which all other aspects of a test event are founded.

Additionally, there are a limited number of samples which can be tested and both funding and test range time are at a premium. However, considering what is at stake; it seems logical to verify a test event’s assumptions, even closely held and historically ironclad assumptions, and to determine a true, overall confidence of a test event’s results to the greatest extent possible. This will not only assist in verifying that legacy systems will continue to operate at optimum levels but this methodology will help fuel and speed the development of future weapon systems. The work presented in this thesis is focused on accurately measuring the delivered thrust of a solid rocket motor as a function of time

to identify changes in performance. These measurements are acquired on a static test stand through the use of load cells. The measurement uncertainty and dynamic response of the system are the main elements of concern.

## B. L-Block Static Fire Test Testing Methodology

For decades, solid and liquid rocket motors have been static fired at the US Army's Redstone Test Center (RTC) test areas as an effective means to ascertain safety, to assess quality, and to evaluate ballistic parameters used in trending and comparative analyses for rocket motor performance and reliability programs. RTC test areas employ 'standard' L-block test stands to static fire solid rocket motors. Several of these L-blocks are mobile while others are fixed at locations within the RTC campus. The mobile L-blocks, an example of which is illustrated in Figure 1.1, are constructed of reinforced concrete and rebar. The baseline measurement train for this study consists of a canister type, strain

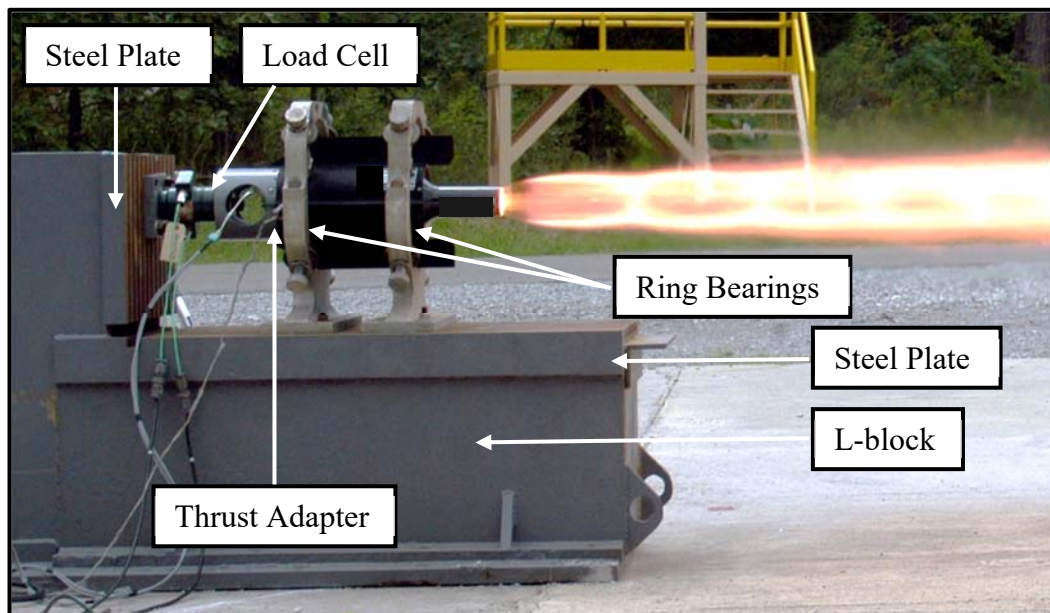


Figure 1.1 Solid Rocket Motor Firing from a Mobile L-block

gauge based load cell (5,000 *lbf*, typical), mild carbon steel thrust adapter which mates the motor to the load cell and allows access to the forward (fwd) motor section, and a pair of ring bearings for centering and leveling purposes. The horizontal 'L' face is fitted with four-inch-thick steel plating while the vertical 'L' face is fitted with two-inch-thick steel plating. The steel plating is embedded with T-type mounting rails on both the horizontal face and the vertical face to allow for the greatest amount of flexibility in mounting test hardware. The mobile L-blocks are employed when firing small, tactical size rocket motors and can be placed at various locations within the RTC campus depending on the overall test schedule and objectives. The fixed L-blocks, see Figure 1.2, are monolithic reinforced concrete / rebar blocks which are embedded below grade (up to 50 feet below grade depending on the L-block in question) and are surrounded by a concrete apron which acts as the L-blocks horizontal 'L' face.



Figure 1.2 Solid Rocket Motor Firing from a Fixed L- block [1]

The vertical 'L' face is covered with a large, six-inch-thick steel plate with various threaded mounting holes in various patterns while the horizontal face employs an I-beam

based rail system which will accept various sized motor firing carts. The measurement train for the fixed L-blocks is almost identical to the mobile L-blocks with the main difference being the magnitude of scale. The test bed for this research effort will be a mobile L-block, however, the results obtained through this analysis can, and will, be applied to all static fire test stands within the RTC campus.

To initiate a static firing test event, a L-block is prepared prior to motor installation. Depending on the motor to be fired, the appropriate load cell, thrust adapter, ring bearings, and other specific attachment hardware are installed on the L-block. Once these items are staged a dimensionally accurate mock motor is installed in order to perform initial centering and leveling with the centerline of the thrust adapter / load cell, see Figure 1.3. This initial centering and leveling is accomplished using three or four (depending on motor to be tested) adjustable cylindrical roller bearings, which allow free axial motion of the motor, threaded through each ring bearing which contact the mock-up motor case and a torpedo level. At the completion of this preliminary centering and leveling process the mock-up motor is removed and a live motor is subsequently installed. After the motor has been inserted into the ring bearings, and just prior to mating the motor with the thrust adapter, the motor's centering and leveling is fine-tuned. This is accomplished by closely monitoring the thrust adapter / motor mating interface just prior to seating the motor into the thrust adapter, see Figure 1.3. The mating interface is brought to within approximately  $1/32^{\text{nd}}$  of an inch and is scrutinized for the presence light, using the naked eye, around the motor's circumference. The thrust adapter / motor is considered leveled and centered when the amount of light around the motor's circumference is evenly distributed. The motor is then seated into the thrust

adapter and bolted in place. At this point, the motor is armed, all personnel retreat to the firing control room, and the motor is static fired, see Figure 1.4. This process is virtually

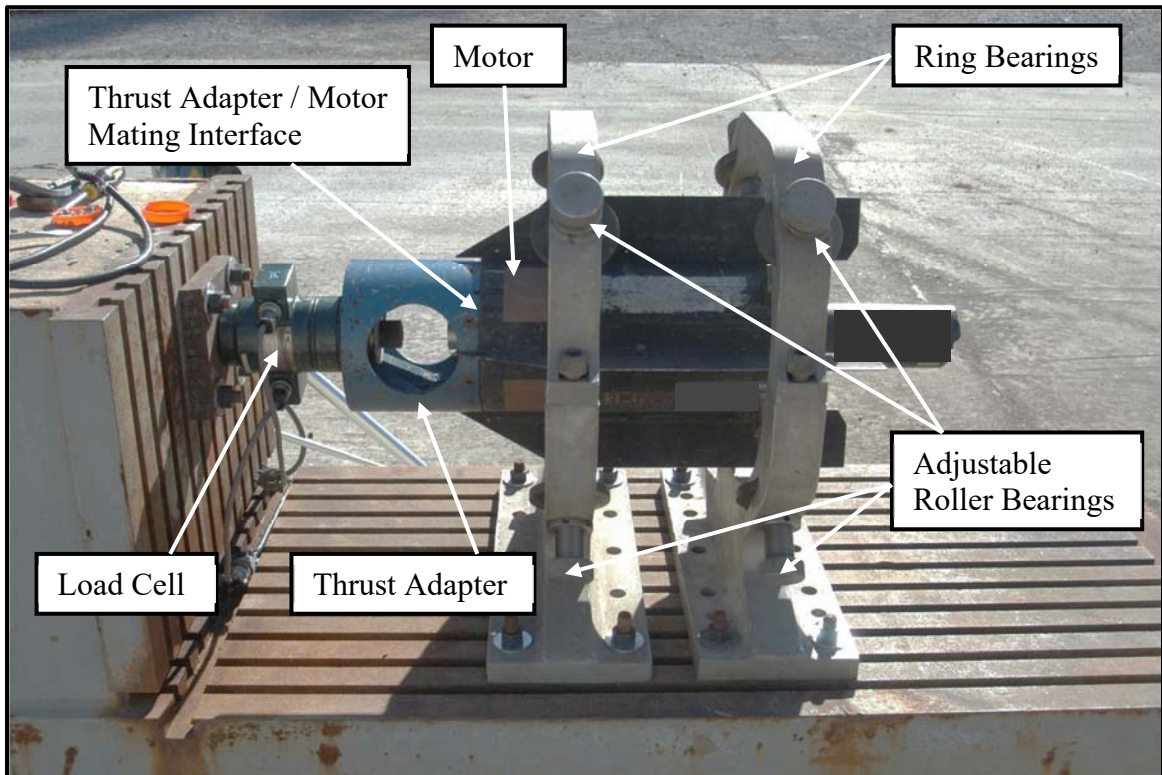


Figure 1.3 Ring / Roller Bearing Arrangement used for Leveling and Centering

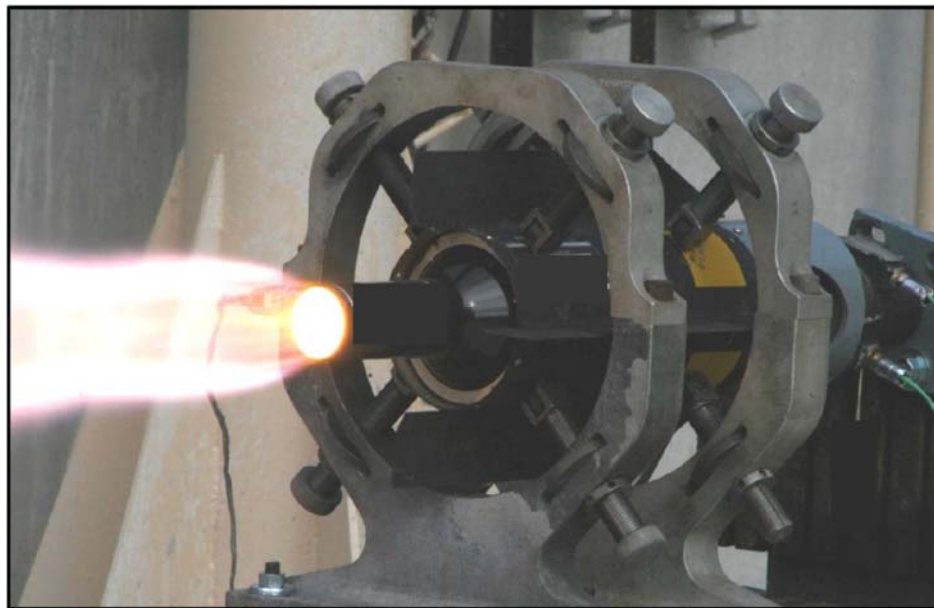


Figure 1.4 Typical Static Motor Firing



the same for all motors static fired at RTC, only the magnitude of scale varies.

Currently, fine tuning a motor's centering and leveling is considered more art than science and is based on years of hands-on field experience in performing this procedure. One intent of this research is to empirically determine the parameters of this hands-on field procedure and quantify its overall effects. This method has been used for decades at RTC and it is theorized that its sufficiency is due, in part, to the fact that overall load cell deflections are typically very slight, ranging between  $8.0 \times 10^{-4}$  and  $7.0 \times 10^{-3}$  inches (*in*) for resident load cells, thereby negating any appreciable effects due to alignment issues.

### C. Load Cells and Measuring Thrust

Due to the inherent lack of clearance and accessibility issues of the L-blocks employed by RTC and the lifecycle of canister type of load cells (barring any catastrophic motor failure that compromises its integrity, this type of load cell can deliver decades of reliable use), RTC employs strain gauge based, canister type load cells to measure thrust data. Thrust, as defined by Webster, is "The forward-directed force developed in a jet or rocket engine as a reaction to the rearward ejection of fuel gases at high velocities" [2], see Figure 1.4. This succinct, yet accurate illustration clearly defines the force, hereto referred to as thrust, generated during the static firing of a rocket motor.

A load cell is a type of transducer that converts a given thrust, to an electrical signal that can be acquired, stored, and analyzed. The magnitude of the electrical signal generated by a load cell is directly proportional to the amount of thrust, applied to its measurement element. The load cell measurement element, see Figure 1.5 [3],

consists of a load path, an elastic body, and a strain gauge. The electrical output of a load cell is based on the phenomenon of resistance variation due to the deflection, elongation in this case, of wire. This ‘wire’ is the modern strain gauge, see Figure 1.6 [4]. As thrust imparts force into the load cell measurement element, the elastic body is compressed and its diameter is slightly increased. This increase in diameter induces a measurable change in resistance due to the elongation effect of the strain gauge, which is bonded to the elastic body, and is subsequently acquired and analyzed. Figure 1.7 is a graphical representation of thrust data generated by a load cell. Due to the sensitive nature of the data used in this research, all data has been normalized.

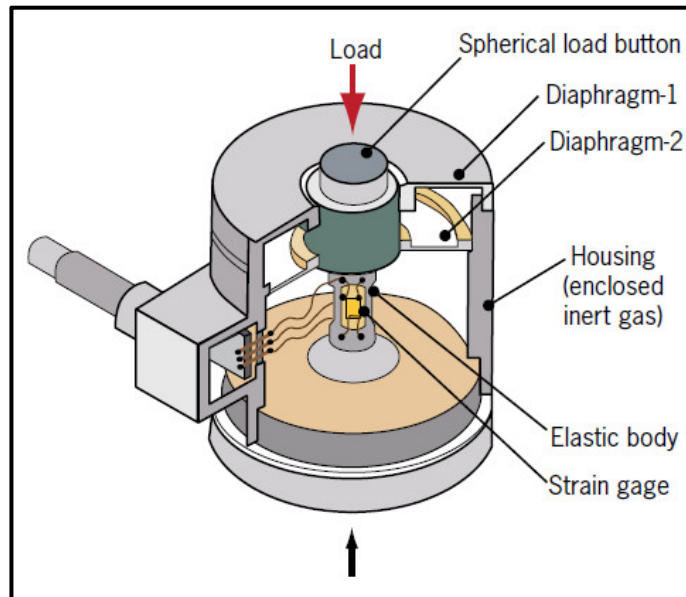


Figure 1.5 Typical Strain Gauge Based, Canister Type Load Cell [3]

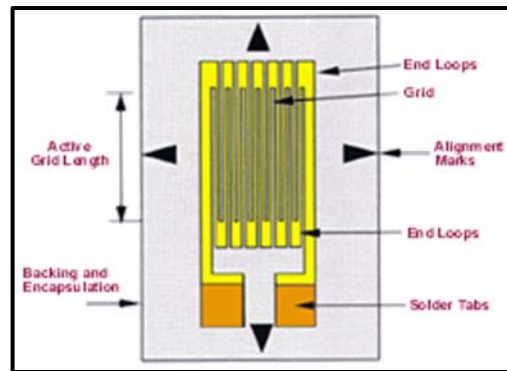


Figure 1.6 Typical Strain Gauge [4]

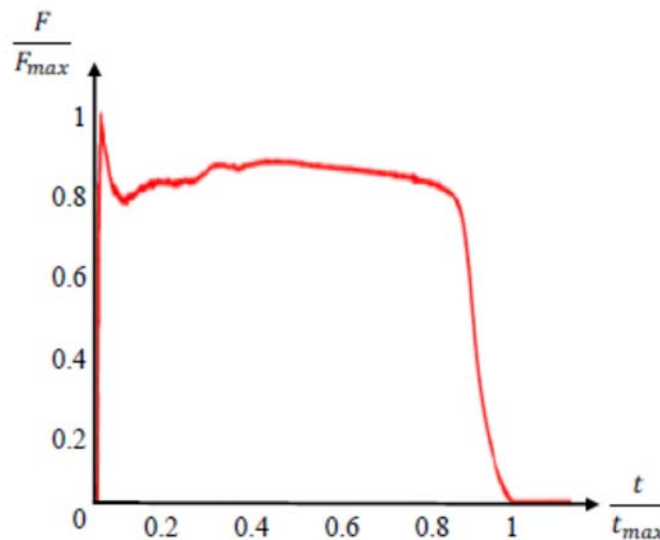


Figure 1.7 Typical Thrust Data Plot

To not oversimplify this process, it should be noted that the plot in Figure 1.7 is the representation of a final thrust curve that would be included in a final report or other publication. This plot is not indicative of the raw data received from a load cell; it was, among other things, low-pass filtered and scaled to the required engineering units.

#### D. Rocket Thrust Measurement Literature Review

Whether for fixed or vectoring nozzles, accurate and realistic measurement of rocket motor thrust has been a topic of discussion for many years. The main components required for the acquisition of thrust measurements are a force measuring transducer (commonly a load cell), a static test stand that captively restrains the motor under test while integrating all the required test equipment, and an alignment system that ensures a true, unencumbered measurement path.

The integrity of the thrust data acquired during testing is critical considering the importance of the decisions based on their results. Consequently, there has been much information presented on the design of static test stands. Zolotorev et al. detail the mechanical setup and construction of a hybrid rocket motor static test stand [5]. Peretz et al. and Rugescu and Sapunaru focused on optimization of feed systems as well as ignition and instrumentation systems of static test stands [6] [7]. Korting and Reitsma evaluated the safety aspects of an indoor test stand including the effects of acoustic noise on the test stand [8]. Thomas et al. discussed the various systems required to operate and interface with a liquid rocket motor test stand [43]. Arrington and Schneider performed work similar to Thomas et al. and also briefly discussed the use of load cells to generate calibration correction curves [45]. Doerksen et al. researched the cost and other physical concerns of a nitrous oxide based, mobile test stand [48]. Finally, Dunn et al. performed finite element analyses on a hybrid rocket test stand to determine maximum yield stresses. This work focused on the top-level designs and entertained only cursory mentions of specific test / data optimization issues.

There have been more focused investigations on static testing of rocket motors, Giligorijević et al. evaluated and tested side forces on a multi axis thrust vector-controlled test stand [9]. Langill and Kapandritis performed evaluations similar to Giligorijević et al. to include the use of flexures to mechanically isolate and aid in aligning the motor, i.e., maintaining low path hysteresis [47]. Favato and Magalhães used finite element analysis to determine structural modes of a liquid bipropellant test stand while varying equipment orientations [10]. Runyan et al. also used finite element analysis to predict test stand structural modes as well applied a one-dimensional spring / mass model to calculate errors in total impulse [44]. Similarly, Spurling et al. employed finite element analysis to determine safety factors, fatigue rates, and repeatability of a test stand used for combustion instability testing [50]. Knauber illustrated the effects that thrust misalignment, e.g., canted nozzle, has on a static test stand [11]. Gerards described a test stand used to test a high pressure, sub-scale motor for burn rate measurements and thrust determinations [12]. Brimhall et al. experimented with a multi axis test stand and ring bearings integrated with sensors to measure misalignment thrust [13]. Stevenson and Lightsey utilized a torsional pendulum static test stand to measure instantaneous impulse and determined that over stiffening the stand structure would degrade the performance of that style test stand [46]. Lastly, Coppotelli and Grappasonni presented a numerical procedure for determining the frequency response of a test stand undergoing a time / mass varying load. Still, this research did not address the nuances of physical test stand setup (e.g., achieving good motor / measurement train alignment) and/or the mitigation of undesirable dynamics.

However, some research has touched on the need to consider certain physical parameters of a static test stand. Renitha and Sivaramapandian speak to the need to design around not only the maximum thrust capacities but the natural frequency of the captive components. A suggested target frequency range, 30-50 Hz, for the components is presented but without a tangible way to logically apply to other static test stands [15]. Kumar and Anjaneyulu discuss many design concerns related to rocket motor testing including the static test stand and the measurement transducer. A natural frequency requirement for the static test stand itself is suggested,  $\leq 4\text{Hz}$ , but it is not corroborated which makes application to other static test stands somewhat difficult. Transducer selection in this work was geared more toward technology, calibration, and survivability than alignment or dynamic considerations [16]. Barber, similar to Kumar and Anjaneyulu, relayed the importance of knowing and controlling the static test stand's natural resonance and, additionally, mentions that the harmonics of a thruster's cycle rate can potentially cause issues with the natural frequency of the thrust transducer. This particular situation does not manifest itself in the type of testing performed at this test area but highlights the importance of ensuring the measurement system is not dynamically compromised [17]. Xing et al. present the dichotomy between thrust measurement sensitivity and frequency response. The design of the thrust measurement device employed in this research is in stark contrast to the canister type load cell used at this test area but the theory of operation is generally the same, the more rigid a measurement system the higher its natural frequency [18]. Finally, Sims and Coleman share an enormous amount insight into large rocket motor alignment for a permanently mounted static test stand. This worked proved path hysteresis is an excellent indicator of

rocket motor misalignments and can be used as a tool to ensure the trueness of coaxial centerlines between a rocket motor and a static test stand [19].

Although similar in some aspects, none of the aforementioned research specifically chronicles the physical setup of a mobile static test stand in regards to alignment and dynamic response of a canister type load cell employed to measure thrust at this test area. This thesis will build on the current knowledge base, identify the major contributors to alignment and dynamic issues in regards to mobile static test stands, and attempt to present a methodology to optimize the acquisition of consistent, accurate, and reliable thrust data from mobile static test stands.

## CHAPTER II

### THE PRINCIPLE OF UNCERTAINTY AND ITS SIGNIFICANCE\*

#### A. Précis on Uncertainty

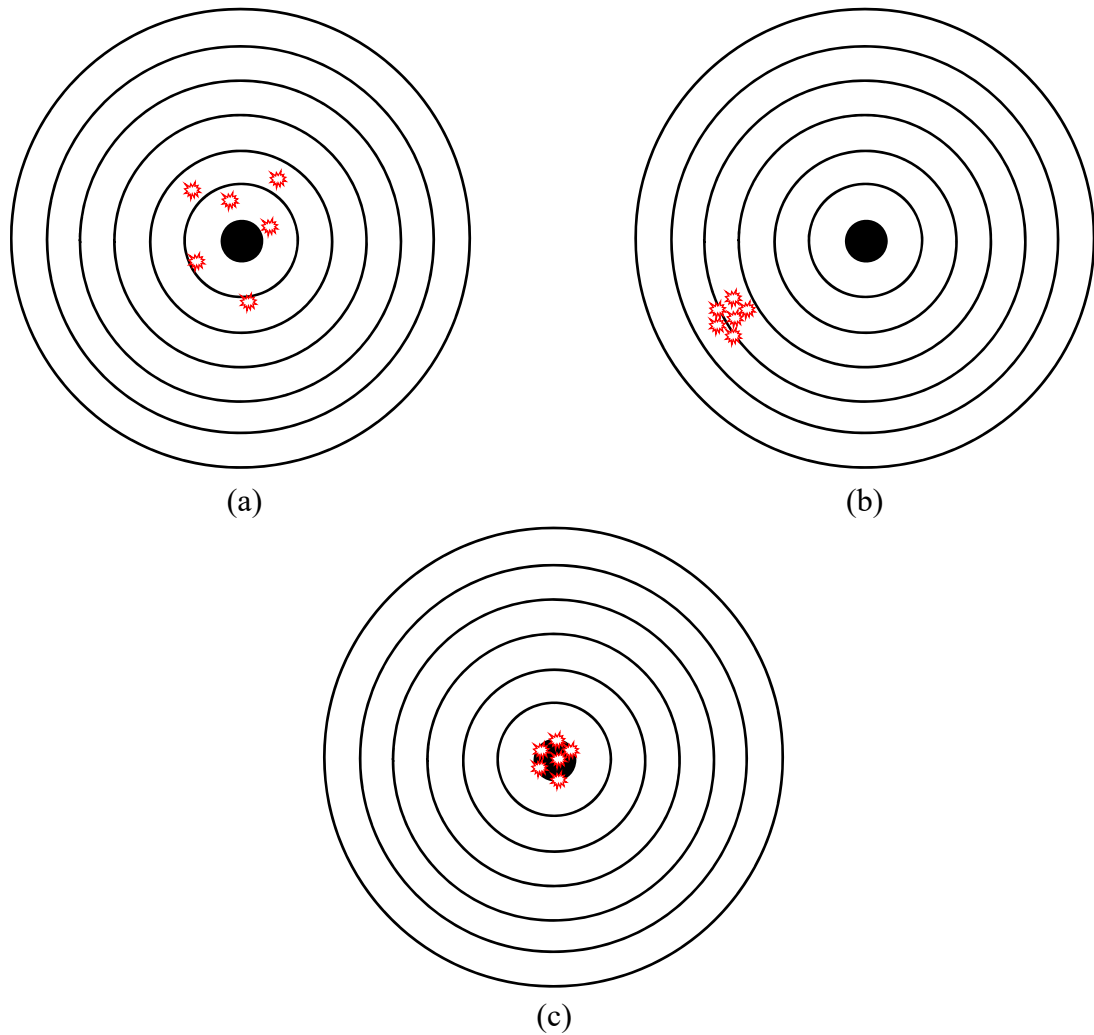
Determining the accuracy and precision of a measurement is an important distinction in thrust measurements. It is widely known that it is very possible to measure accurately but not precisely. Conversely, it is also possible to very precisely measure an inaccurate value. What is missing from this conundrum is the certainness of the measurement in which the evaluator has interest. The relative certainness of a measurement is rather peculiarly referred to as measurement ‘uncertainty’. Uncertainty is, by its very definition, being in a state of doubtfulness or unknowingness. With regards to a measurement, this can be condensed to the following, simple question: how ‘good’ is the measurement in reference to its real-world value. In the realm of Research, Development, Test, and Evaluation (RDT&E) it is sometimes very difficult, if not impossible, to envision the phenomena being measured (e.g., strain or acceleration). As a result, there are built-in uncertainties that must be addressed before a level of confidence can be levied upon a measurement. The following illustrations will attempt to emphasize the importance of determining measurement uncertainty.

Figure 2.1, (a) through (c), illustrates groupings that could be encountered on a target during bullet or fragment impact testing.

---

\* This chapter has been adapted from references [20] and [21]





(a) Accurate but poor Precision, (b) Precise but poor Accuracy, and (c) Accurate and Precise

Figure 2.1 Accuracy versus Precision

In Figure 2.1 (a), the evaluator is acutely aware of the accuracy and precision from this vantage point and sees a relatively accurate but not very precise result. Comparatively, the evaluator can ascertain from Figure 2.1 (b) that while there is good precision, the accuracy leaves much to be desired where Figure 2.1 (c) illustrates an ideal result. The advantage the evaluator has in regards to the certainty of accurately and precisely hitting the target's bullseye is the ability to 'see' the target and make adjustments based on

where successive rounds or fragments impact the target. However, as evaluators of phenomena that cannot be ‘seen’, the visual acuity and certainty in ensuring the bullseye is hit translates into a measure of uncertainty and confidence levels since the true real-world value (target) can never be truly measured (seen). This difference between the true and measured value is commonly referred to as error. As a result, the evaluator is blind to the effective error in Figure 2.1 (a) and the error between Figure 2.1 (b) and (c). This illustrates the importance of determining a measurement’s uncertainty; so that the quality of a measurement, or its estimated error range, may be adequately evaluated and properly considered.

#### B. The Utility of Uncertainty

Uncertainty, as an analysis tool, can help assure the evaluator that the value of a measurement falls within an estimated error range, at some level of confidence, with respect to the true real-world value. To sufficiently define the estimated errors required in calculating the uncertainty of a measurement, it will be necessary to deconstruct and define the components that compose the estimated errors of a measurement and how, or if, they correlate. Uncertainty, is divided into two types, A and B. Type A is based on statistical analysis of objectively measured samples of data whereas Type B is based on statistical analysis of empirical or heuristic data, its distribution is based on experience and knowledge of the process, and tends to be more subjective than Type A. The estimated, or total, error is defined as the sum of the random and systematic errors (historically known as precision and bias error, respectively). Figure 2.1 (a) illustrates a random error where as a systematic error is illustrated between Figure 2.1 (b) and (c).

Additionally, for the purposes of this research, normal (Gaussian) distribution and the Large Sample Assumption (LSA) are assumed unless otherwise noted. The LSA states that for the vast majority of engineering measurements, where the population is typically large ( $\geq 31$  samples), the Student's *t-distribution*, or just *t-distribution*, for 95% ( $2\sigma$ ) and 99% ( $3\sigma$ ) confidence levels may be assumed to be 2 and 2.6, respectively. For populations that contain 30 and fewer samples the *t-distribution* value will need to be determined to properly calculate confidence level coverage factors.

A random standard error,  $\varepsilon$ , affects the value of a measurement in differing amounts during a test event and cannot be predicted based previous or historical results. It is seen in the data as scatter, See Figure 2.1 (a) and Figure 2.2. In this way, most random errors are typically uncorrelated, or independent of one another, and tend to vary with time. In the past, correlated random errors have been assumed to be zero and therefore ignored. However, this practice should be used with caution as random errors can, at times, be correlated. A systematic standard error,  $\beta$ , affects the value of a measurement equally throughout a test event, does not tend to vary with time, and cannot be seen in the data. This fact makes systematic errors particularly worrisome to the evaluator. In fact, it is easy to see that if a measurement is relatively precise (low scatter) the evaluator can be lured into a false sense of security in regards to the validity of the measurement (precisely measuring an inaccurate result), see Figure 2.1 (b) and Figure 2.2.

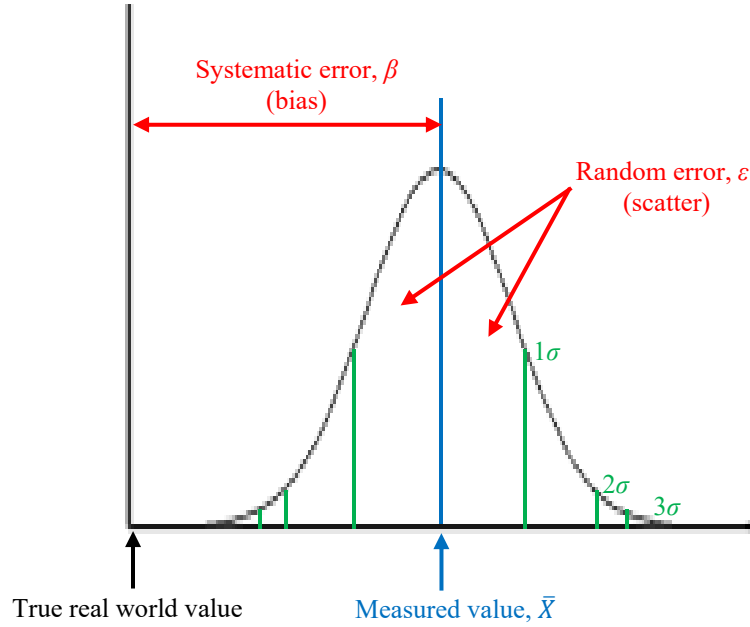


Figure 2.2 Error Relationship between a True Value and its Measured Value

In contrast to random errors, systematic errors are more prone to being correlated or dependent upon one another (although not a requirement). For example, if a single device is used to make multiple measurements its systematic error will be distributed across and influence all the measurements made with that device.

It is worthy to note that random and systematic errors are additive

$$Err_t = \varepsilon_n + \beta_n \quad (2.1)$$

where  $Err_t$  is the total error,  $\varepsilon_n = (\varepsilon_1 + \varepsilon_2 + \dots + \varepsilon_n)$ , and  $\beta_n = (\beta_1 + \beta_2 + \dots + \beta_n)$ . Using this fact, the true real-world value is defined as the sum of the measured value and the total error

$$T_v = M_v + Err_t \quad (2.2)$$

where  $T_v$  is the true real-world value and  $M_v$  is the measured value. However, this result only reveals a portion of what is required to quantify the quality of a measurement.

There must be a range defined where each error source, whether random or systematic, is expected to fall. Mathematically speaking, this estimated range around the error sources is defined as standard uncertainty,  $u$ , and is the sum of the standard uncertainties of each individual error source.

$$u = u_1 + u_2 + \dots + u_n \quad (2.3)$$

Although this result may seem trivial it provides a pathway to a very powerful analytical tool.

Before further investigating the application of random and systematic standard errors and their uncertainties it is prudent to first briefly discuss and obtain some insight into the mathematics required to calculate errors of this type. Type A random error,  $\varepsilon$ , calculation is based on normal distributions (see Figure 2.2 for a representative plot of Equation 2.4)

$$f(x) = \frac{1}{\sigma\sqrt{2\pi}} e^{-(x-\mu)^2/2\sigma^2} \quad (2.4)$$

where  $f(x)$  is the frequency of a measurement within a normal distribution,  $e$  is the natural logarithm base,  $x_i$  is a value in the normal distribution,  $\mu$  is the average of the normal distribution, and  $\sigma$  is the standard deviation of the normal distribution defined as,

$$\sigma = \lim_{N \rightarrow \infty} \left[ \sqrt{\sum \frac{(x_i - \mu)^2}{N}} \right] \quad (2.5)$$

where  $N$  is the number of samples. The probability of measuring a specific value in a normal distribution, within the bounded portion of a population set,  $\tau$ , is defined as the Cumulative Distribution Function (CDF),  $\Phi$ ,

$$\Phi(\tau) = \frac{1}{\sqrt{2\pi}} \int_{-\tau}^{\tau} e^{\left(\frac{-\tau^2}{2}\right)} \delta_{\tau} \quad (2.6)$$

where,

$$\tau = \frac{\Delta X}{\sigma} \quad (2.7)$$

It should be noted that Equations 2.4 and 2.5 are based on access to an infinite population of samples. An evaluator will never have access to an infinite population set. Therefore, the evaluator is relegated to using the available population set. The standard deviation,  $s_x$ , and the mean standard deviation,  $s_{\bar{x}}$ , of finite population sets are defined as,

$$s_x = \sqrt{\frac{\sum_{j=1}^N (X_j - \bar{X})^2}{v}} \quad (2.8)$$

$$s_{\bar{x}} = \frac{s_x}{\sqrt{N}} \quad (2.9)$$

Where  $\nu$ , or  $(N - 1)$ , is the sample set's degrees of freedom (DOF),  $X_j$  is the value of the  $j^{\text{th}}$  sample, and  $\bar{X}$  is the average of the sample set. Equation 2.8 defines the scatter, or random error, of a sample set that occurs about  $\bar{X}$  as depicted in Figure 2.2. Equation 2.9 then describes the average scatter of the sample set that occurs about  $\bar{X}$ .

Type B systematic error,  $\beta$ , unlike Type A random error is consistently present in successive measurements, equally biases a measured value throughout a measurement, and cannot be detected by the evaluator (e.g., calibration errors), see Figure 2.2. This fact illustrates why it is very important to consider the effect of systematic error sources during any test event measurement.

Most processes are multivariate. To calculate the value of a specific variable a mathematical expression that defines the behavior of that specific variable in relation to the other process variables must be generated. Coleman and Steele [20] define this expression as a Data Reduction Equation (DRE).

$$r = r(X_1, X_2, \dots, X_i) \quad (2.10)$$

Where  $r$  is the 'result' and  $(X_1, X_2, \dots, X_i)$  are the relevant process variables. Keep in mind that each process variable contains its own random and systematic errors that will propagate through the calculated result and must be tracked. Therefore, all the errors must be evaluated to determine the uncertainty of the result. The summation of these errors leads to an estimate of the result's standard uncertainty

$$u_r = \sqrt{(\varepsilon_r^2 + \beta_r^2)} \quad (2.11)$$

where

$$\varepsilon_r^2 = \sum_{i=1}^j \left( \frac{\delta r}{\delta X_i} \right)^2 \varepsilon_{X_i}^2 \quad (2.12)$$

$$\beta_r^2 = \sum_{i=1}^j \left( \frac{\delta r}{\delta X_i} \right)^2 \beta_{X_i}^2 \quad (2.13)$$

and  $\left( \frac{\delta r}{\delta X_i} \right)$  is the partial derivative of each variable in the DRE.

However, there is still an important component missing, a confidence interval. For the aforementioned calculations to be truly useful there has to be some level of confidence in what is being calculated or, rather, confidence that a measurements value will fall within a defined interval. Once this confidence interval is determined and is combined with the total error, a true measure of uncertainty can be attained. The expanded uncertainty at 95% confidence,  $U_{95\%}$ ; using the LSA; then becomes,

$$U_{95\%} = 2u_r \quad (2.14)$$

There are also the possibility of correlated (dependent) errors in both random and systematic standard uncertainty calculations. Correlated random and systematic errors physically manifest themselves in different ways. A correlated random error, for example, could be realized when two transducers used to make an averaged measurement



both encounter variances during a measurement process. In regards to these same transducers, a correlated systematic error could result from the transducers being calibrated using the same calibration process. Since correlated errors are dependent they bring with them covariance factors which predict how the errors (a variable) vary in relation to one another. If errors tend to vary in the same ‘direction’, this implies a positive covariance. Conversely, when errors tend to vary in an opposite ‘direction’, this implies a negative covariance. A positive covariance increases uncertainty whereas negative covariance reduces uncertainty.

Equipped with this insight a complete picture of uncertainty can now be formulated. Considering  $2\sigma$  constraints, i.e., 95% coverage, expanded uncertainty of a result can now be defined as

$$U_{r,95\%} = E_r^2 + B_r^2 \quad (2.15)$$

where,

$$E_r^2 = \sum_{i=1}^j \left( \frac{\delta r}{\delta i} \right)_i^2 (E_i)^2 + 2 \sum_{i=1}^{j-1} \sum_{k=i+1}^j \left( \frac{\delta r}{\delta i} \right)_i \left( \frac{\delta r}{\delta k} \right)_k C_{E_{ik}} E_i E_k \quad (2.16)$$

using LSA,

$$E_i = 2s_x \quad (2.17)$$

where  $C_{E_{ik}}$  is the correlation coefficient for random errors and,

$$B_r^2 = \sum_{i=1}^j \left( \frac{\delta r}{\delta i} \right)_i^2 (B_i)^2 + 2 \sum_{i=1}^{j-1} \sum_{k=i+1}^j \left( \frac{\delta r}{\delta i} \right)_i \left( \frac{\delta r}{\delta k} \right)_k C_{B_{ik}} B_i B_k \quad (2.18)$$

where  $C_{B_{ik}}$  is the correlation coefficient for systematic errors.

Examination of a notional, general case DRE will help the evaluator visualize the functional form of an uncertainty analysis and how the errors propagate. Keeping the number of process variables to two, for simplicity's sake, and using Equation 2.10 as inputs into Equation 2.15, at a 95% confidence level,

$$\begin{aligned} U_{r,95\%} = & \left( \frac{\delta r}{\delta X_1} \right)^2 E_{X_1}^2 + \left( \frac{\delta r}{\delta X_2} \right)^2 E_{X_2}^2 + 2 \left( \frac{\delta r}{\delta X_1} \right) \left( \frac{\delta r}{\delta X_2} \right) C_{E_{ik}} \\ & + \left( \frac{\delta r}{\delta X_1} \right)^2 \beta_{X_2}^2 + \left( \frac{\delta r}{\delta X_2} \right)^2 \beta_{X_1}^2 + 2 \left( \frac{\delta r}{\delta X_1} \right) \left( \frac{\delta r}{\delta X_2} \right) C_{\beta_{ik}} \end{aligned} \quad (2.19)$$

The thrust values presented in this research were directly measured using a single load cell, were not corrected with a pretest calibration curve, and were not derived from a process equation. Therefore, the uncertainties for these thrust measurements lie within the instrumentation equipment and the load cells used to acquire and analyze the thrust data. As a result, DRE development was not required for this effort. However, the DRE discussion presented above is beneficial to the evaluator as it provides valuable insight into how process variables influence one another and how this influence propagates through a measured process.

### C. Rocket Thrust Measurement Uncertainty Literature Review

Measurement uncertainty estimates have become a requirement for many technical publications and enhance the reliability, and even believability, of theoretical results and empirical data per Meyn [22]. Typically, for rocket motor testing, there is an extreme amount of effort put into a test's setup, execution, and teardown. Unfortunately, the data acquired from this process is often treated as an afterthought. When the time comes to analyze the data it is tabularized, plotted, labeled, and handed to those who funded its acquisition with no real concern about the "goodness" of the data. This is due, in part, to dependence on calibrated equipment and transducers and well-established legacy policies and procedures. In the past there was no requirement to calculate the goodness, or the uncertainty, of the acquired data but rather the data had to simply fall within a plus and minus error percentage of some expected range. Fortunately, this mindset is changing and the importance of uncertainty analysis is becoming widely accepted at this test area.

Analogous to the critical nature of thrust data acquisition integrity, the uncertainty estimates of this acquired data is of equal importance [23]. It seems reasonable, considering the amount of effort and attention to detail required to accurately and precisely measure thrust, that the same rigor be applied to determining the goodness of the acquired data. There has been many papers and books written concerning uncertainty and its calculation. This specific work discusses how uncertainty should be generally applied to both theoretical endeavors, where a process DRE may be developed, and empirical studies where data is directly acquired; but it does not specifically address the unique case of thrust data acquisition from a static test stand [20] [21] [22] [23]. More specific research using data obtained from the static testing of rocket motors, Chunfu's et

al. presentation of static thrust line measurements [24] and Temple's et al. discussion of data acquisition uncertainty [25], briefly mentions equipment uncertainties that should be considered in relation to the specific research being performed but is still somewhat vague on the topic. Dauch reported on the uncertainty of propellant burn rate measurements which included an analysis of measurement equipment (e.g., a pressure transducer and a caliper) and data acquisition system digitization delays [26]. Sims and Sims and Coleman performed detailed uncertainty analyses of thrust measurements on a large-scale liquid rocket motor static test stand. This analysis revealed that alignment and load cell uncertainties were the major contributors to thrust measurement uncertainty [27] [28]. Finally, Frederick and Greiner as well as Sims and Coleman presented advanced uncertainty analyses of several rocket motor performance parameters including fuel regression rates, oxidizer flux, characteristic velocity, and oxidizer-to-fuel mass ratio. Although this research is well outside the scope of this thesis it is further proof of the increased need and importance of uncertainty analysis estimates [29] [30].

The aforementioned research was used as the basis for determining how to best measure the uncertainty of a mobile static test stand in regards to direct thrust measurements. This thesis will build on the current knowledge base and identify the major contributors to the uncertainty of direct thrust measurements while using mobile static test stands.

## **CHAPTER III**

### **THRUST MEASUREMENT STUDY**

The objective of this thrust measurement study was to challenge all previous assumptions; investigate the validity of currently employed equipment, methods, and procedures; and determine the areas where uncertainty affects the ‘goodness’ of acquired thrust measurements. To accomplish this objective an active mobile static test stand with motor appropriate fixtures and load cell was employed to investigate dynamic effects and determine how alignment and calibration procedures influence the characteristics of a thrust measurement. Similarly, the signal conditioning and data acquisition systems were analyzed to determine their role in affecting thrust measurement acquisition.

#### **A. Dynamic Effects**

Historically, at this test area, the data acquired from rocket motor static firing tests have been analyzed solely in the time domain with little or no emphasis placed on frequency-based analysis. The frequency response of the fixtures and the resulting mechanical pathways encountered during these tests were of little, if any concern. Fixtures were generally regarded as no more than a captive component of the test and not as an integral part of the data collection process. As a result, and to varying degrees, many thrust curves generated contain a “ringing” component. Depending on the frequency of this ringing, it could be attributed to electrical noise. Resolving this type of ringing is relegated to investigating overall electrical / instrumentation cabling maintenance, grounding techniques, power conditioning, and managing cable lengths

/ configurations. However, at other frequencies where the values did not fit nicely into a harmonic of electrical noise, mechanical resonances were identified as the possible source. Without benefit of the high-end modeling and analysis tools that are now readily available; the simple principle of compression, through the use of in-house fabricated preload-rigs, was employed in an attempt to ‘tighten’ and tune-out unwanted mechanical resonances. Currently, preload-rigs are still in use at this test area.

A preload-rig for a tactical size rocket motor consists of a flat, straight metal bar with two holes at each end and is bolted, through the holes / compression springs, over the load cell sensing button to the L-block, see Figure 3.1.



Figure 3.1 Preload-Rig for a Tactical Size Rocket Motor

Typically, for a small tactical motor configuration with known ringing issues, a 2,000 *lbf* preload is applied to the load cell prior to firing. This is not a trivial task as the preload is applied to each side of the rig, sequentially, by tightening the adjustment

nut on the attachment bolt, just above the compression springs, a number of revolutions on one side and then replicating this process on the other side. This back and forth adjustment continues until the predetermined preload is achieved. This procedure requires close attention-to-detail and coordination with the setup technicians and the control room operators to ensure the preload is physically balanced and evenly distributed across the load cell's load button so no side loads are induced. Depending on the experience level of the technicians and the operators, this procedure can take 20-60 minutes per motor. For test days where multiple motors must be fired, this added requirement noticeably affects test efficiency especially since the preload must be verified prior to each firing. Additionally, this delay is of particular concern for temperature conditioned motors that carry time sensitive reconditioning requirements.

The success of the preload-rig is, admittedly, limited as its effectiveness varies between different motor types and tends to even vary within subsequent testing of the same type motor. The use of this rig nominally compresses, i.e., 'tightens', the measurement train driving the overall system's natural resonance frequency up but it does not completely remove the ringing components in the band of interest (usually between 500-1,000 *Hz*). While this procedure 'reduces' the ringing presented in the thrust plots in the band of interest it, subsequently, reduces the overall usable range of the load cell by the preload value. For small motor firings that midrange a particular load cell, this fact may necessitate the use of a larger capacity load cell to ensure the maximum range of the load cell's measurement element is not exceeded. Higher capacity load cells require larger and bulkier mounting equipment and are more

difficult to handle. Although this becomes more of an issue during large rocket motor testing, it can still cause setup issues and delays during small rocket motor testing.

As a consequence, a general analysis of overall system dynamics was initiated to determine any measurable effects on the data collected and to devise a more practical and scientific way to resolve the aforementioned dynamic response concerns. To this end, an empty, inert, and dynamically accurate tactical size rocket motor was staged in a ready-to-test configuration on a portable L-block, shown in Figure 3.2. This configuration was instrumented with modal accelerometers, in several key locations, and a modal impact hammer was used to impart a known forcing function at several areas of interest, see Figure 3.3.

Analysis of the resulting modal data is presented in Figure 3.4. It can be seen that there is no appreciable dynamic influence from the ring / roller bearing captive component of this test setup at the motor or load cell/ thrust adapter locations. This seems to suggest that resonances due to the captive fixturing are well outside the band of interest for the test setup employed at this test area. Further, it is hypothesized that the existence of any higher frequency components from the captive fixturing, if they exist, will largely be attenuated due to decoupling effects at the roller bearing interfaces. The data acquired on the fwd end of the motor, at the thrust adapter / motor interface, indicates the motor itself is slightly influenced by the resonate response of the load cell / thrust adapter arrangement. For the datasets that captured this resonance, their values are at least an order of magnitude below what is seen at the thrust adapter. This too is most likely attributed to decoupling effects at the thrust adapter / motor interface.



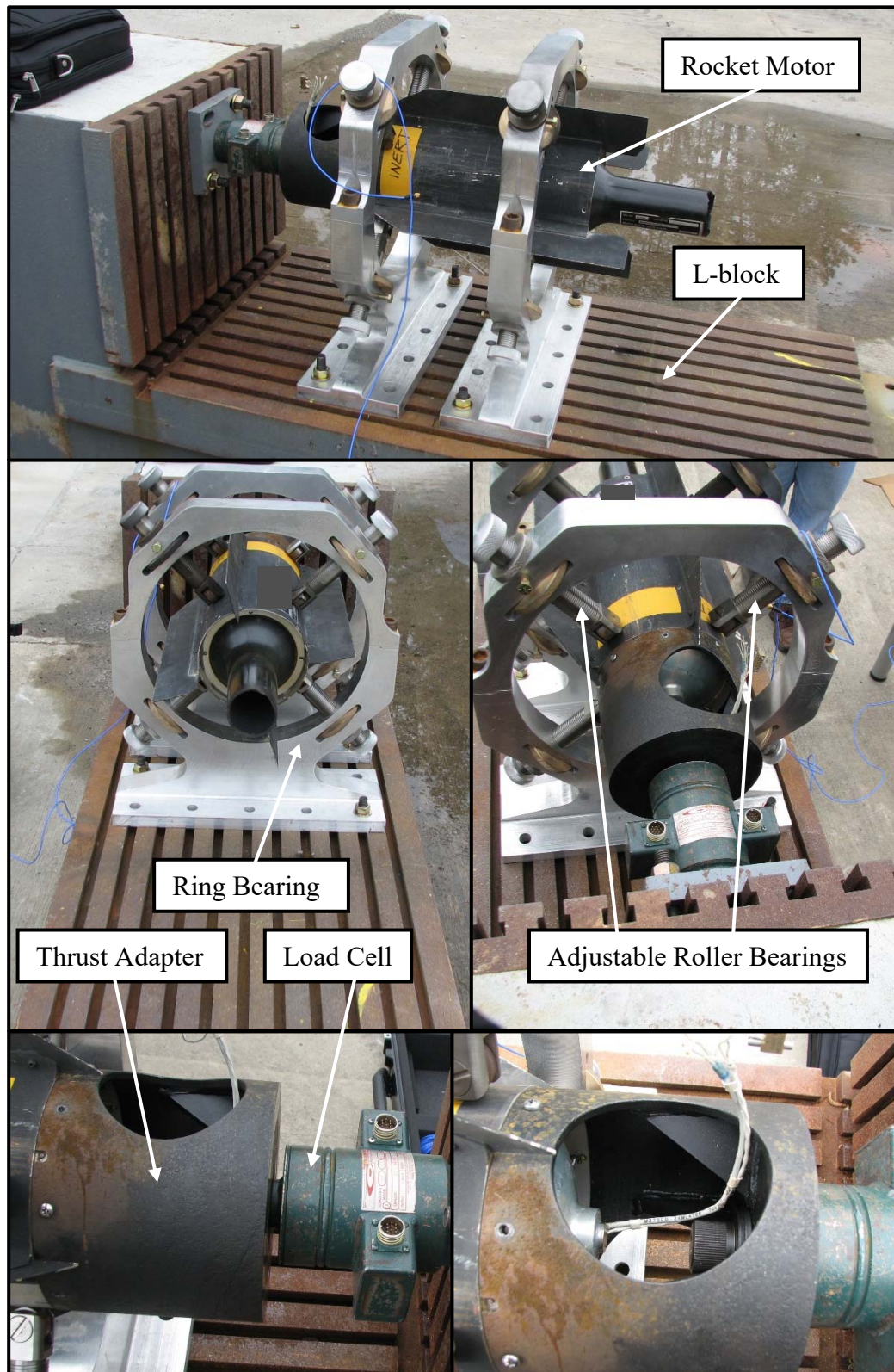


Figure 3.2 Static Firing Configuration for an Inert, Tactical Size Rocket Motor



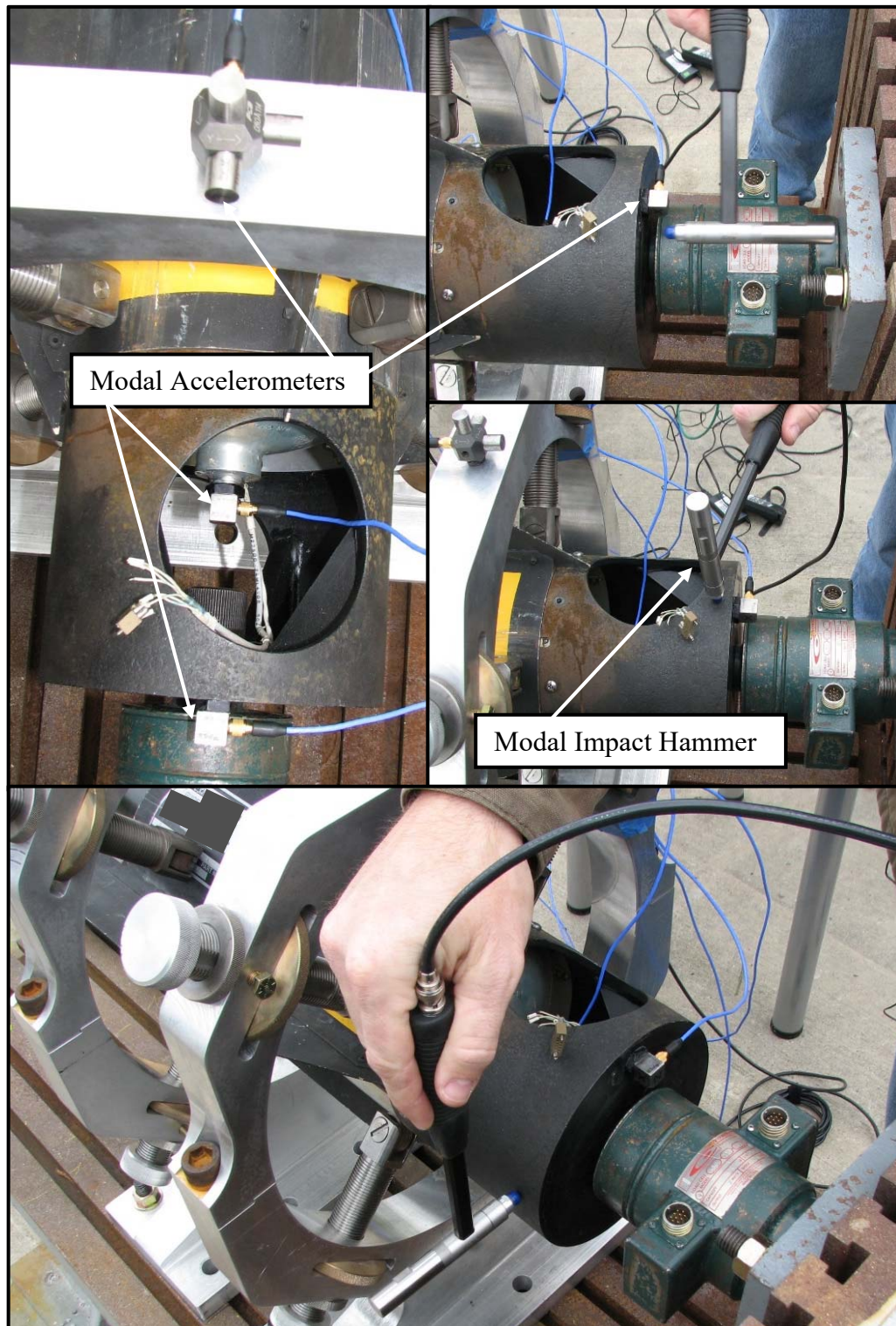


Figure 3.3 Modal Accelerometer Placement and Example Impact Locations

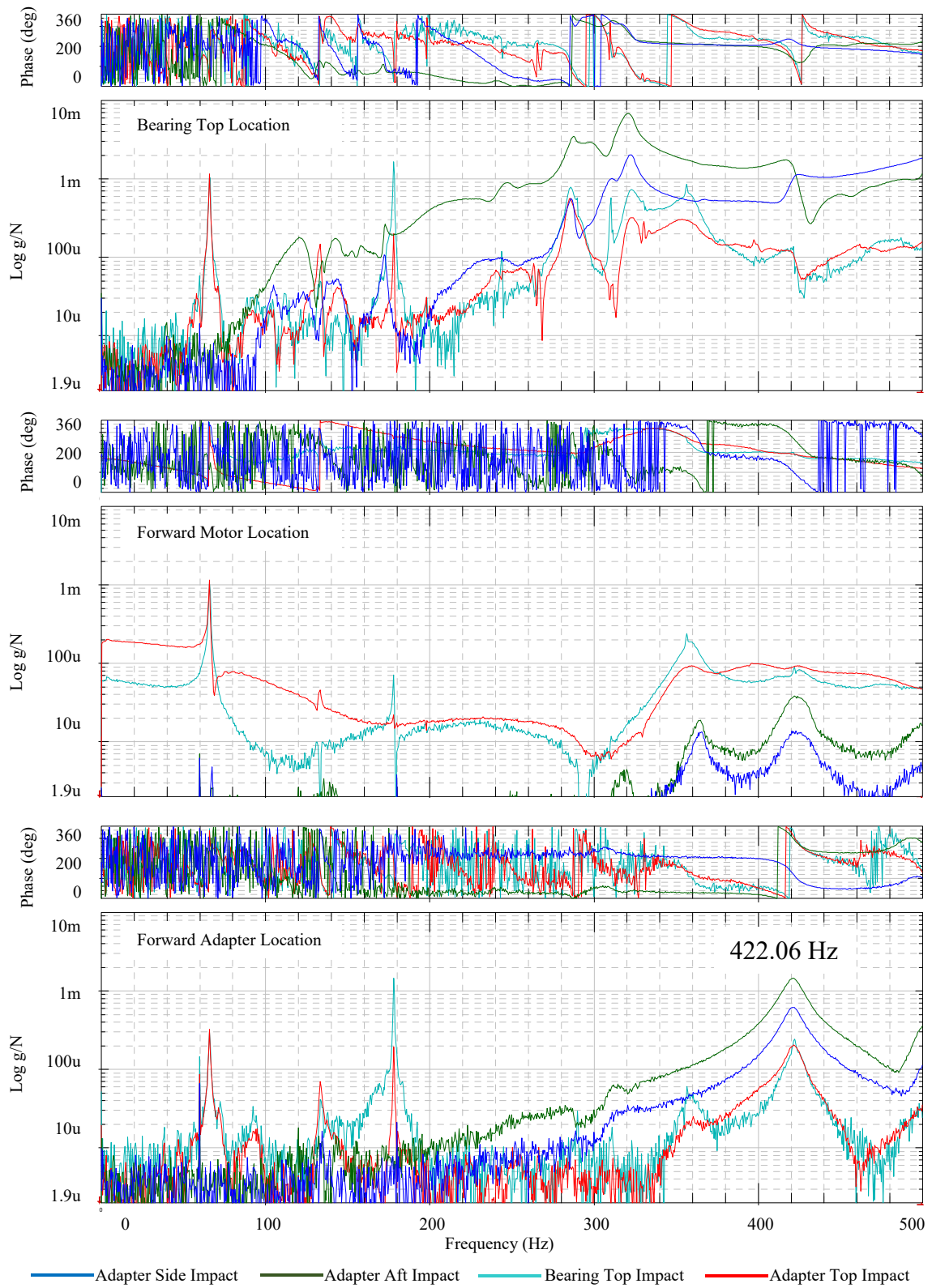


Figure 3.4 Modal Analysis Results of the Tactical Size Rocket Motor Setup

Further investigation into the modal data revealed that, by far, the main and dominate driver for ringing in the thrust data collected during mobile L-block static firings was due to the frequency response of the load cell. The natural resonant frequency,  $f_n$ , of a load cell can be expressed as an undamped, one-dimensional, second order lumped model based on a spring-mass system using Hooke's Law and simple harmonic motion

$$f_n = \frac{1}{2\pi} \sqrt{\frac{k}{m}} \quad (3.1)$$

The Spring Constant,  $k$ , according to Hooke's Law, is defined as

$$k = \frac{F_{spring}}{d_{spring}} \quad (3.2)$$

where,  $F_{spring}$  is the load applied to the spring and  $d_{spring}$  is the deflection of the spring. The amount of mass attached to the spring,  $m$ , is defined as

$$m = \frac{w}{g} \quad (3.3)$$

where,  $w$  is the weight and  $g$  is the gravitational constant. For a canister type load cell, assuming the load cell is a rigid body, Equation 3.1 becomes

$$f = \frac{\sqrt{g}}{2\pi} \sqrt{\frac{k}{w_e + w_l}} \quad (3.4)$$

where,  $w_e$  is the mass of the load cell's moving measuring element and  $w_l$  is the mass of the attached load. Further, since the mass of the attached load decreases as the motor's propellant burns Equation 3.4 becomes

$$f = \frac{\sqrt{g}}{2\pi} \sqrt{\frac{k}{w_e + (w_l - w_p \frac{d}{dt})}} \quad (3.5)$$

where,  $w_p$  is the mass of the propellant. Per Equation 3.5, the load cell's resonant frequency is time variant. As a result, to determine the optimal load cell frequency response range, the maximum resonant frequency point (empty motor) and the minimum resonant frequency point (full motor) for an approximated tactical size rocket motor were calculated and are presented in Table 3.1.

Table 3.1 Calculated Load Cell Resonance Frequencies for an Approximated Tactical  
Size Motor Static Fire Test

Load State	$k$ (lbs/in)	$w_e$ (lbs)	$w_l$ (lbs)	$w_p$ (lbs)	Approximate Frequency (Hz)
Pre-fire (Full Motor)	$7.0 \times 10^5$	1.5	36.5	20.0	344
Post-fire (Empty Motor)	$7.0 \times 10^5$	1.5	36.5	0.0	425

The post-fire frequency approximation in Table 3.1 closely correlates to the dominate frequency revealed in the modal data, see Figure 3.4, and further validates the load cell's dominate effect on acquired thrust data.

To further illustrate this phenomenon, a generic small rocket motor thrust curve is presented in Figure 3.5 prior to any digital filtering or manipulation.

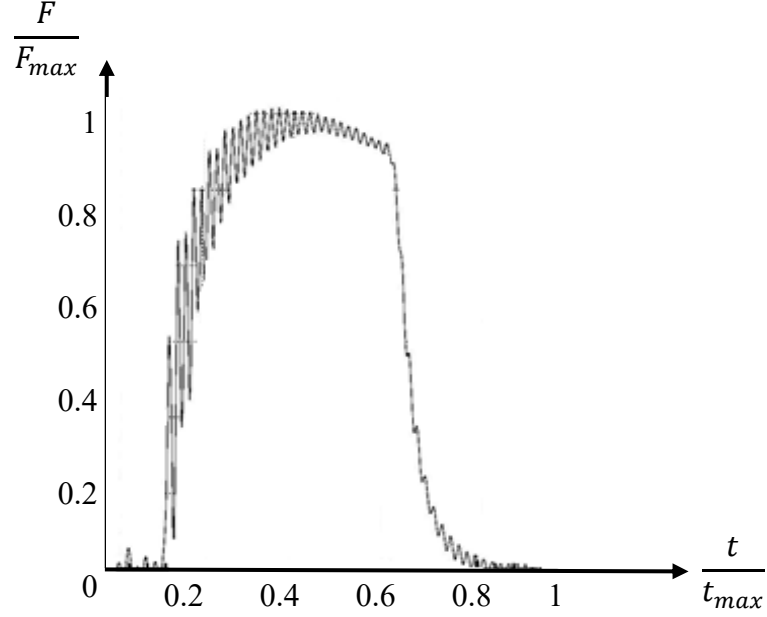


Figure 3.5 Characteristic Ringing in a Generic Thrust Plot

Readily apparent from Figure 3.5, the ringing component dominates the thrust curve's landscape and distorts any potential features of interest. Although the ringing is not a pure sinusoid, its frequency can be roughly estimated by inverting the time differential,  $\Delta t$ , between subsequent peaks using

$$f = \frac{1}{\Delta t} \quad (3.6)$$

Plot analysis tools, available in the employed data acquisition system, were used to determine the time differential between two, randomly selected subsequent peaks at the static fire's initial rise and final tail-off, see Table 3.2.

Table 3.2 Estimated Load Cell Ringing Frequency from an Actual Tactical Sized Motor

Static Fire Test

Thrust Plot Analysis Location	Peak Differential (s)	Peak Frequency (Hz)	Approximate Frequency (Hz)	Damping Ratio, $\zeta$
Initial Rise (Full Motor)	0.00323	309.6	344	0.32
Final Tail-Off (Empty Motor)	0.00242	413.2	425	0.17

The damping ratio,  $\zeta$ , is defined as

$$\zeta = \sqrt{1 - \frac{f_{peak}}{f_{approx}}} \quad (3.7)$$

where  $f_{peak}$  is the peak frequency estimated from actual thrust data using Equation 3.6 and  $f_{approx}$  is the frequency calculated from Equation 3.5. The small  $\zeta$  for the empty motor condition is an indication of a lightly damped system, is the response expected from an axial thrust measurement made with a load cell, and adds further validity to the peak and approximated frequency's physical agreement. A comparison of the data in Figure 3.4, Table 3.1, and Table 3.2 reveal a relatively close correlation between the modal, approximated, and actual load cell (albeit estimated) resonance frequencies for tactical size rocket motors fired at this test area.

In an attempt to further optimize design and mitigate dynamic effects of the load cell / thrust adapter arrangement, two theoretical thrust adapters as well as the legacy thrust adapter were modeled and contrasted in ANSYS using two, fully defined active bodies

(load cell and thrust adapter). The load cell was assumed to be a single-part, rigid body but the overall model's geometry stiffness was considered flexible. Table 3.3 lists the frequency of the first four modes. Figure 3.6 through 3.8 depict dominate mode 3 of each thrust adapter and illustrates that the maximum response for this mode is located at the adapter face, i.e., at the thrust adapter / motor interface.

Table 3.3 Thrust Adapter Weight and Frequency for the First Four Mode Shapes

Mode	Thrust Adapter 1		Thrust Adapter 2		Legacy Adapter	
	<i>Hz</i>	<i>lbs</i>	<i>Hz</i>	<i>lbs</i>	<i>Hz</i>	<i>lbs</i>
1	305.25	3.9828	322.95	3.7662	289.73	15.286
2	309.32		324.06		291.79	
3	481.23		473.41		422.06	
4	1082.30		994.16		1158.80	

It can be seen that reducing the thrust adapter mass by approximately 75% did not appreciably increase the frequency content of Mode 3, the dominate load cell natural frequency seen in the thrust data. This fact further validates the overall governing effect of load cell dynamics on thrust measurement in this configuration. Based on this analysis the effort to redesign and manufacture a new thrust adapter was abandoned.



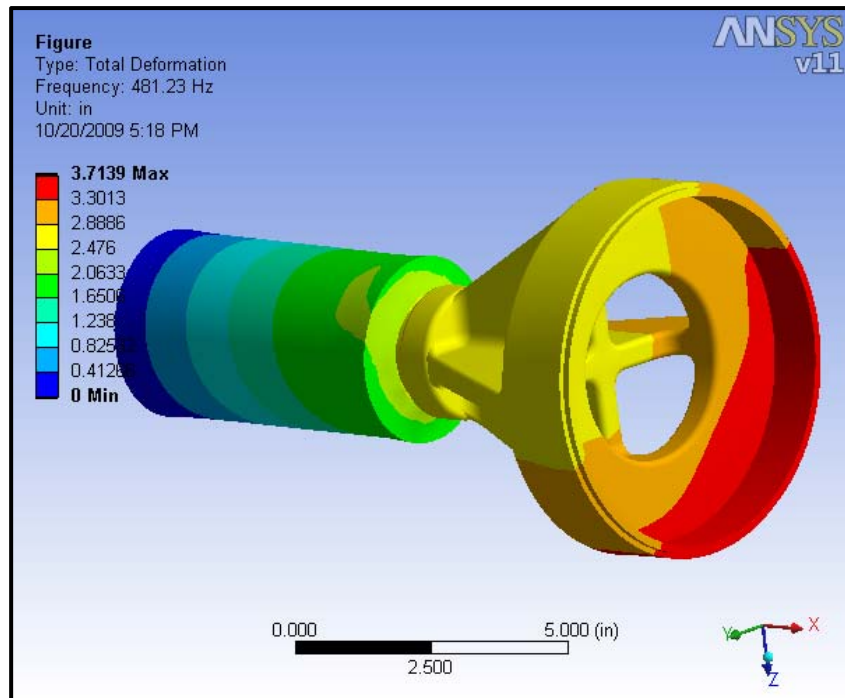


Figure 3.6 Theoretical Thrust Adapter 1, Dominant Mode 3

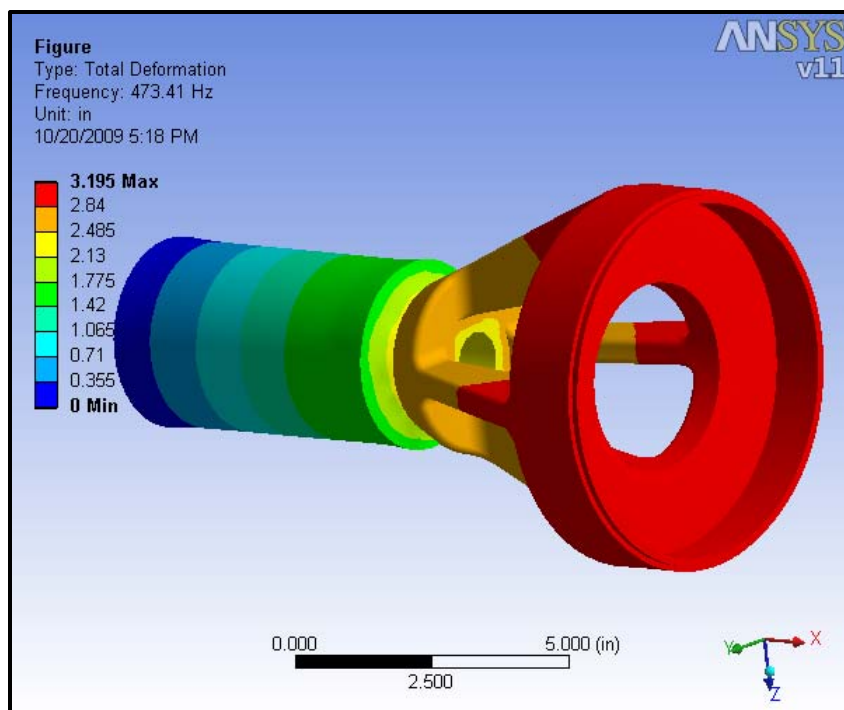


Figure 3.7 Theoretical Thrust Adapter 2, Dominant Mode 3

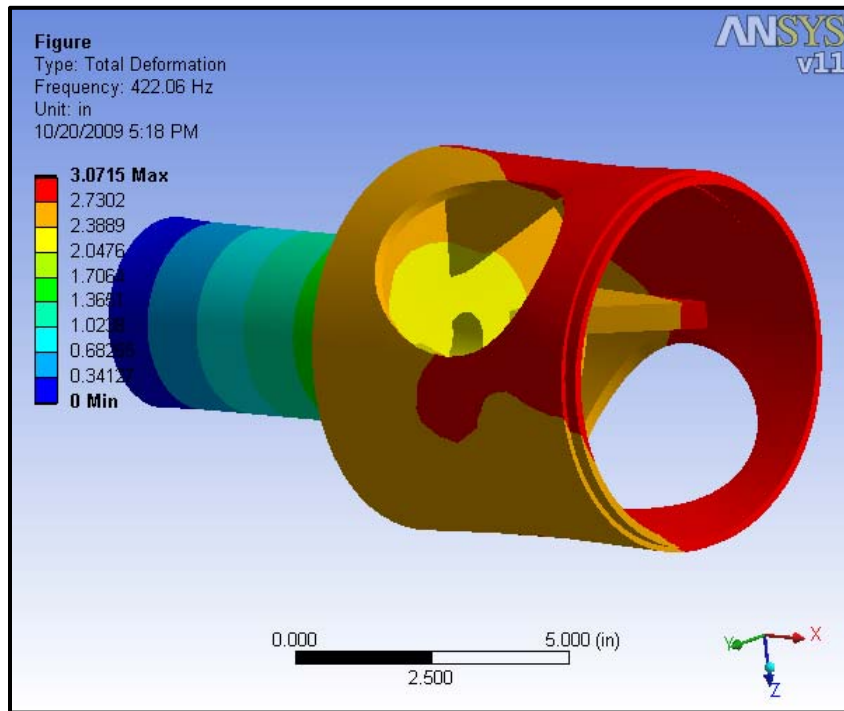


Figure 3.8 Legacy Thrust Adapter, Dominate Mode 3

Although acquired thrust data can be post-processed and ‘cleaned-up’ to remove the ringing (e.g., through averaging or filtering); these techniques either smear, distort, or eliminate data altogether. Regardless of the technique employed, the original dataset is modified or portions removed to dispense with undesirable or troublesome characteristics. These modifications may mask or altogether eradicate real world phenomena that occur during a live fire event. None of these options are ideal and are very problematic to both the evaluators who generate this data and the customers that ultimately consume said data.

To resolve this dynamic response issue, a cooperative research project was initiated with industry to design and construct a load cell with dynamic characteristics more

conducive to static testing of tactical size rocket motors at this test area. Taking into account the preload-rig concept and the aforementioned load cell resonance calculations, it was determined that the simplest and most direct way to increase a load cell's natural frequency is to increase its spring constant, i.e., stiffness. Although there is a finite amount a spring constant can be increased, due to load cell material and mechanical properties, the increase required for this application was deemed achievable. After consulting with an OEM concerning physical and electrical constraints, a new load cell was designed and constructed. The legacy and new load cell design, hereto referred to as the "new design", are shown in Figure 3.9.



Figure 3.9 Load Cell Comparison

The legacy and new design's pertinent physical parameters are presented in Table 3.4. To determine the effectiveness of this new design a series of test firings, on the same type of tactical rocket motor previously discussed, was initiated without the use of a preload

rig. Figure 3.10 and Figure 3.11 are a representation of the raw thrust data acquired from similar motor type firings using a legacy load cell and the new load cell design, respectively.

Table 3.4 Comparison of Load Cell Design Parameters

Parameter	Legacy [31]	New Design [32]
Maximum Deflection	0.007 <i>in</i>	0.0008 <i>in</i>
Maximum Load	5,000 <i>lbs</i>	10,000 <i>lbs</i>
Spring Constant (calculated)	$7 \times 10^5$ <i>lbs/in</i>	$12.5 \times 10^6$ <i>lbs/in</i>
Measurement Element Weight	1.5 <i>lbs</i>	1.23 <i>lbs</i>
Resonant Frequency (no load, calculated)	2,160 <i>Hz</i>	10,000 <i>Hz</i>
Resonant Frequency (empty motor case, calculated)	425 <i>Hz</i>	1761 <i>Hz</i>
Resonant Frequency (full motor case, calculated)	344 <i>Hz</i>	1435 <i>Hz</i>

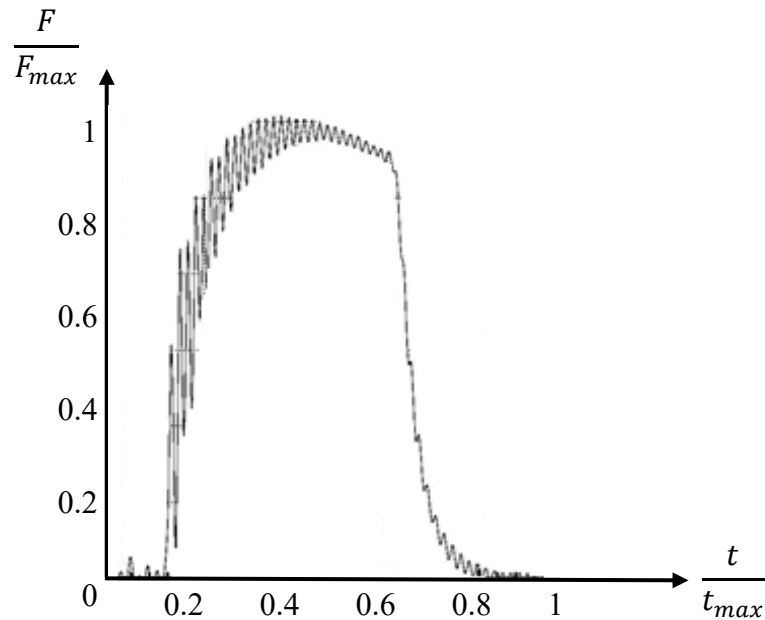


Figure 3.10 Raw Thrust Data Acquired from a Legacy Load Cell

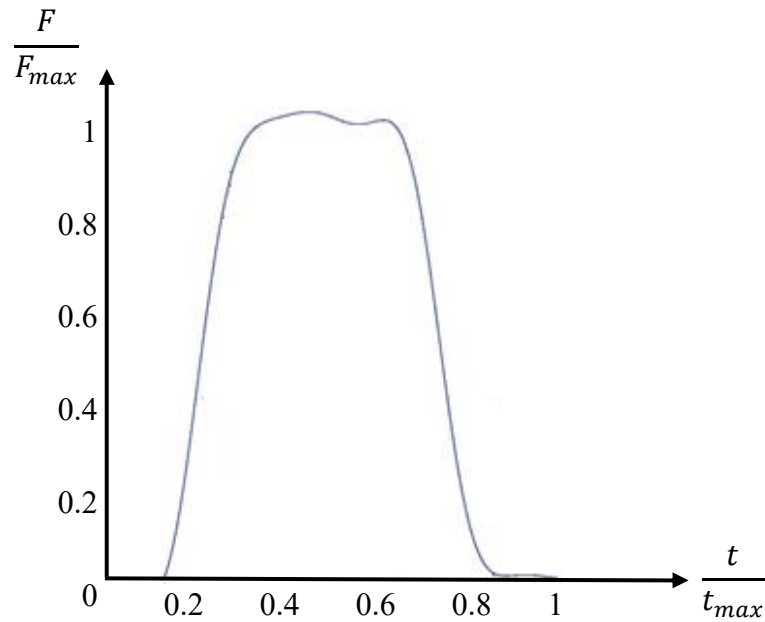


Figure 3.11 Raw Thrust Data Acquired from the New Design

Through examination of Figure 3.10 and Figure 3.11 it is readily apparent that there is much less distortion of the thrust curve when using the new design. Additionally, the ability to identify real-world thrust curve phenomena is enhanced due to a much higher fidelity curve and realistic landscape, see Figure 3.12. These enhancements will not only increase test efficiency, since preloading will no longer be required, but they will significantly increase the accuracy and consistency of calculating required ballistic parameters while helping to facilitate continued automation efforts for these calculations.

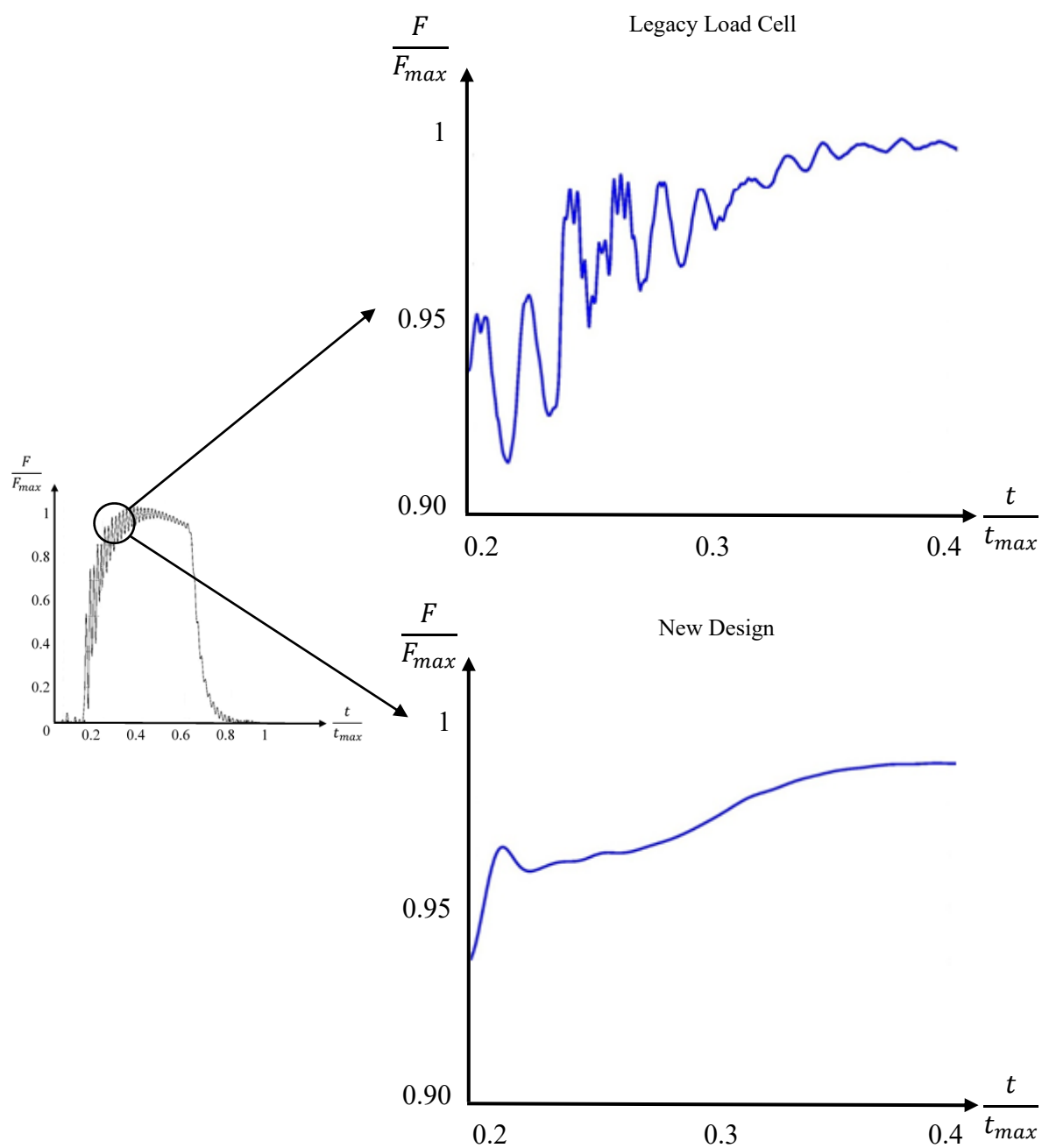


Figure 3.12 Thrust Curve Detail Comparison, Legacy Load Cell versus the New Design

## B. Motor Alignment

The test stand employed for this empirical study is a mobile L-block. While the very nature of this stand allows for the greatest flexibility in regards to where and when a test can be executed, its down side is the potential lack of consistent alignment. As mentioned in Chapter I, the motor alignment in relation to this test stand is subjective. Centering and leveling are referenced to the spatial characteristics of the L-block each time it is moved and relocated. This fact renders the use of a separate centering and leveling system impractical due to additive losses in time and funding. It is much more prudent to continue utilizing the current procedures if proven to be sufficient and not appreciably adding to the overall uncertainty of the test results.

Prior to installing the static fire test hardware and determining the sufficiency of this test area's centering and leveling procedures, the measurement uncertainty due to operator biases of the Twin Beam Dial Gauge (TBDG) used to measure centering and leveling values was determined. The L-block was moved under cover, placed on a reasonable flat and level surface, and a generic height measurement was iterated ten times after a baseline measurement was acquired, see Figure 3.13. These measurements were acquired at ten-minute intervals and were alternated between two experienced operators. Since the L-block mounting surfaces and TBDG are both of steel construction, their coefficients of thermal expansion are assumed to be essentially equal negating any potential measurement effects due to thermal fluctuations. In light of the methodology employed by this test area's centering and leveling process, it is assumed that variations in pitch and yaw of the motor, relative to the axial axis of the motor, will be similar in magnitude. As a result, only relative pitch measurements were obtained.

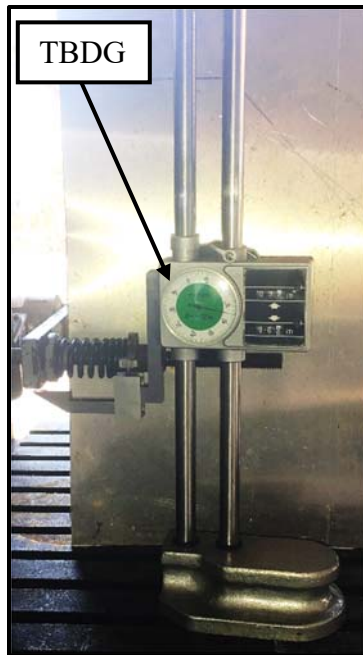


Figure 3.13 Setup to Determine the TBDG Measurement Uncertainty

Based upon the aforementioned parameters and assumptions, TBDG uncertainty is composed of three main error sources: gauge measurement resolution, operator perspective, and variations due to repetitive gauge measurements. Since it is not known which side of the true value these errors will fall and since the relative size of these errors is difficult to estimate, some assumptions will need to be applied to the calculations. The TBDG is an analog instrument and literature [20] suggests that for an analog reading (e.g., graduated scales, tick marks) the assumed measurement uncertainty should be half of the least scale division or  $5.0 \times 10^{-4} \text{ in}$  for this gauge [33]. It is safe to assume this type of error follows a relatively uniform model since the reading will fall within the scaled divisions. The uncertainty of an analog reading error,  $u_{are}$ , can be estimated with the following [34]



$$u_{are} = \frac{M_{lim}}{\sqrt{3}} \quad (3.8)$$

where  $\sqrt{3}$  is an artifact of the uniformly distributed error model.

Operator perspective errors present themselves in several ways and are not easily quantified or mathematically modeled. Examples of this type of error are inconsistent gauge placement, viewing angle (in regards to reading scales or dials), subjectivity, and fatigue. Based on application of past experiences and assuming a normal distribution, the uncertainty of evaluator error,  $u_{ee}$ , can be estimated with the following [34]

$$u_{ee} = \frac{M_{lim}}{\phi^{-1}\left(\frac{1+C_L}{2}\right)} \quad (3.9)$$

where  $M_{lim}$  is the measurement limits,  $\phi^{-1}$  is the Inverse CDF (ICDF), and  $C_L$  is the desired confidence level.  $M_{lim}$  may be set at half the resolution of the least scale division of the gauge or  $5.0 \times 10^{-4}$  in for this TBDG. However, experience with this TBDG has shown that increments of  $2.5 \times 10^{-4}$  in can be consistently attained by experienced operators. Lastly, it should be noted that  $\phi^{-1}$  cannot be calculated directly. Nonetheless, values for  $\phi^{-1}$  can be found in statistics books, programs, or through internet-based calculators.

The average uncertainty introduced through repetitive TBDG measurements,  $u_{\overline{rme}}$ , is determined by Equation 2.8 and 2.9. Using Equation 2.11, the resultant measurement uncertainty,  $u_{r,meas}$ , of the TBDG can now be calculated,

$$u_{r,meas} = ([u_{are}]^2 + [u_{ee}]^2 + [u_{\overline{rme}}]^2)^{\frac{1}{2}} \quad (3.10)$$

With the uncertainty of the TBDG measurements calculated, the DOF must be estimated in order to properly apply a confidence interval. The estimated number of DOF, or  $\nu_{est}$ , can be determined using the Welch-Satterthwaite equation [20]

$$\nu_{est} = \frac{u_r^4}{\sum_{i=1}^j \left( \frac{u_i^4}{\nu_i} \right)} \quad (3.11)$$

Table 3.5 is a summary of the TBDG measurement uncertainty calculation results.

Table 3.5 TBDG Measurement Uncertainty Calculation Results

$u_{are}$ (in)	$u_{ee}$ (in)	$u_{\overline{rme}}$ (in)	$u_{r,meas}$ (in)	$\nu_{est}$ (DOF)
$2.89 \times 10^{-4}$	$1.28 \times 10^{-4}$	$6.72 \times 10^{-5}$	$1.31 \times 10^{-3}$	$1.3 \times 10^6$

Since  $\nu_{est}$  is well above the LSA, the *t-distribution* coverage factor for 95% confidence will be assumed to be two. In light of the aforementioned results, the 95% confidence level for the TBDG height measurement can now be expressed using

$$Meas \pm t_{95\%} u_r \quad (3.12)$$

Therefore, the confidence interval for the TBDG height measurement is

$$9.00213 \text{ in} \pm 0.00262 \text{ in} \quad (3.13)$$

This result indicates a high level of reliability and accuracy can be garnered from using the aforementioned TBDG and, subsequently, provides confidence in the validity of the relative alignment measurements outlined and acquired below.

At the conclusion of the TBDG uncertainty procedure, the load cell and thrust adapter were installed and leveled in reference to the horizontal surface of the L-block. The ring bearings were then mounted onto the L-block and a mock motor was installed and macro centering and leveling were initiated. The mock motor was removed, a wait time of ten minutes was observed, and the mock motor was reinstalled. At this point fine centering and leveling procedures were initiated. Upon completion, baseline pitch measurements of the fwd and aft ends of the mock motor were obtained using the TBDG, see Figure 3.14. The mock motor was again removed, a ten-minute pause was observed, the mock motor was the reinstalled, fine centering and leveling procedures were initiated, and pitch measurements were reacquired. This procedure was iterated ten times and was alternated between two experienced operators. This iteration scenario best replicates a reasonably average test day for ambient, tactical size rocket motor static fire testing at this test area. The relative mock motor measurement results are presented in Table 3.6 and illustrates a high level of consistency and effectiveness from this field procedure for the alignment of small rocket motors as evidenced by the near-zero residual estimated angle. However, by themselves, consistency and effectiveness do not tell the entire story. The final piece is the quality of this alignment linking the rocket motor and the load cell. Measurement path hysteresis, the difference between the readings, or path, of a load as it

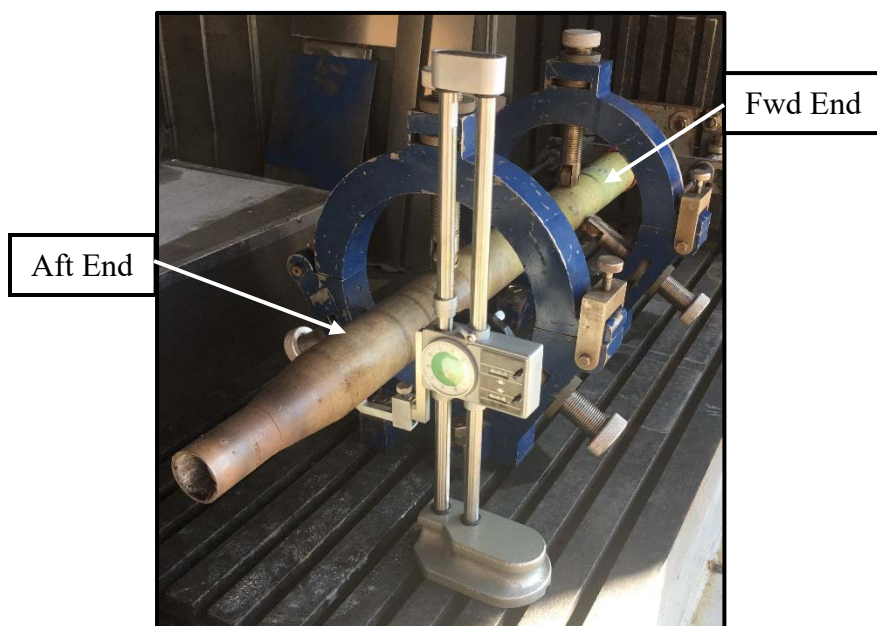


Figure 3.14 TBDG Mock Motor Measurement Setup

Table 3.6 Relative Mock Motor Height Measurements

Sample	Motor Pitch (14 inches between Fwd and Aft Measurement Locations)						
	Fwd (in)	Fwd Baseline $\Delta$ (in)	Aft (in)	Aft Baseline $\Delta$ (in)	Fwd-Aft $\Delta$ (in)	Estimated Slope	Estimated Angle $^{\circ}$
Baseline	9.6025		9.6		0.0025	1.79E-04	1.02E-02
1	9.6025	0.0	9.605	0.005	0.0025	1.79E-04	1.02E-02
2	9.6	0.0025	9.6075	0.0075	0.0075	5.36E-04	3.07E-02
3	9.6025	0.0	9.605	0.005	0.0025	1.79E-04	1.02E-02
4	9.5975	0.005	9.6	0.0	0.0025	1.79E-04	1.02E-02
5	9.6	0.0025	9.6025	0.0025	0.0025	1.79E-04	1.02E-02
6	9.6025	0.0	9.6075	0.0075	0.005	3.57E-04	2.05E-02
7	9.6025	0.0	9.6075	0.0075	0.005	3.57E-04	2.05E-02
8	9.605	0.0025	9.6075	0.0075	0.0025	1.79E-04	1.02E-02
9	9.6025	0.0	9.5975	0.0025	0.005	3.57E-04	2.05E-02
10	9.6025	0.0	9.6025	0.0025	0.0	0.00E+00	0.00E+00

is being increased versus being decreased, is a good indication of alignment quality for this type of test item. As a result, a hysteresis plot was generated using the aforementioned field alignment procedures and a hydraulic ram. The setup was once again replicated but, due to the rarity and cost of the mock motor, the mock motor was replaced with a hydraulic ram and a preload-rig was added as a passive safety attachment device between the ram / mock thrust adapter and the load cell, see Figure 3.15. The mock thrust adapter was custom manufactured for use with the ram and was designed to match the mating tolerances between an actual thrust adapter and a rocket motor. This allowed the ram to be centered and leveled using the same aforementioned procedures. Once positioned the opposite end of the ram was flush mounted to a prepositioned, 10,000 *lb*, steel faced reaction mass using spacers and shims. A 3,000 *lbf* load was then applied to the load cell and subsequently released. Figure 3.16 is a hysteresis plot generated after the load was applied and released from the load cell.

Although this test area does not use hydraulic loads to make pretest alignment changes or generate calibration correction factors, Figure 3.16 demonstrates that the difference in input path and output path was only about 0.22%. Consequently, the employed motor alignment procedure, at least for small, tactical size rocket motors, is quite good and does not require any major modifications at this time. This somewhat surprising result is due, in large part, to many decades of operator experience and many years of trial-and-error. It remains to be seen if this procedural talent can be passed on to the next generation's workforce.

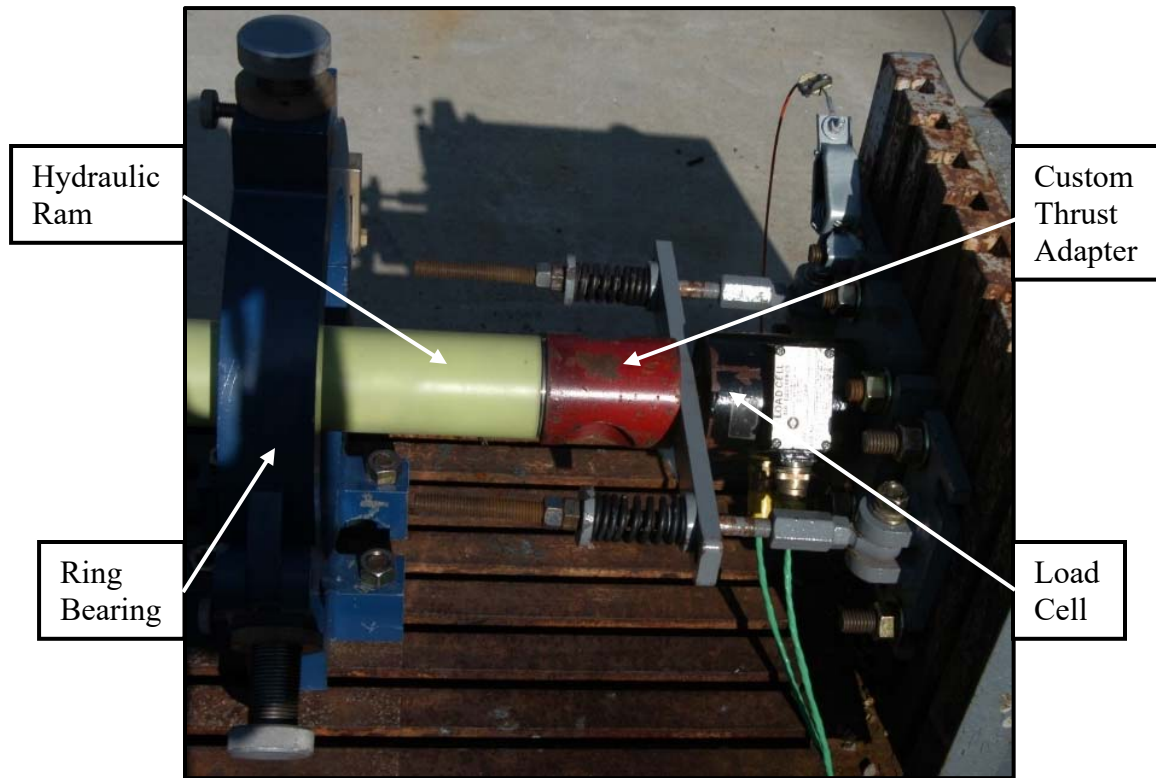


Figure 3.15 Load Cell Loading Setup

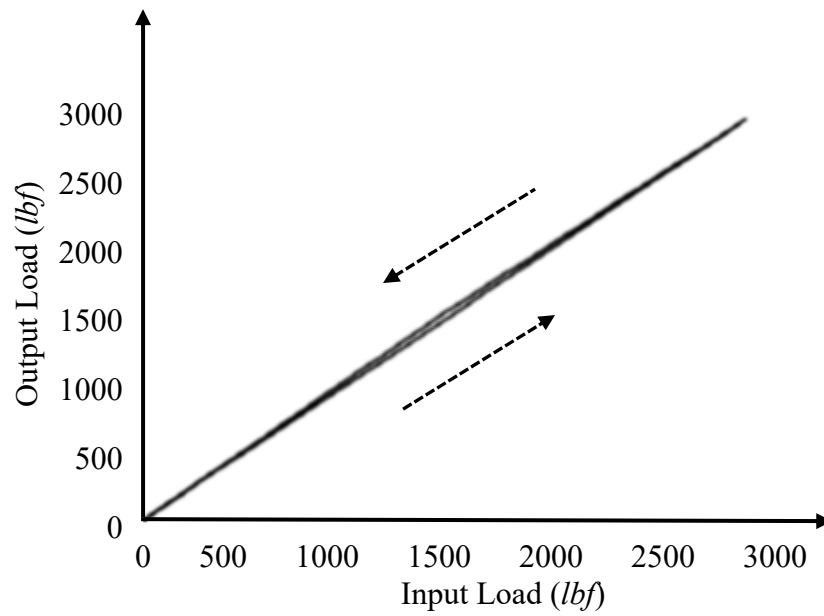


Figure 3.16 Measurement Path Hysteresis

### C. Signal Condition System (SCS)

The SCS employed for testing and experimentation at this test area is used to filter and amplify transducer signals mounted to and / or near an item under test. When these signals are filtered and amplified, errors are introduced due to ambient electrical noise and the SCS's internal circuitry that must be defined and quantified. The SCS OEM uses their own internal, Factory Acceptance Testing (FAT) using National Institute of Standards and Technology (NIST) traceable calibration equipment to calculate the overall uncertainty of their measurement equipment, see Appendix A for further details. The goal of the OEM's FAT is to assure a Test Uncertainty Ratio (TUR) of 4:1 for all critical measurements and provide the evaluator with confidence in using the published SCS specifications. It should be noted that most quality calibration laboratories hold a 4:1 TUR as their target control point since it maintains the delicate balance between predicting the probability band of in tolerance measurements and cost realism. Although higher TURs are possible, there is a significant cost increase for generally only a modest widening of the probability band for a given measurement. As a result, the OEM's published specifications will be used to calculate the total SCS uncertainty for strain gauge based load cell thrust measurements acquired at this test area. A simplified channel block diagram is presented in Figure 3.17 which illustrates the measured signal's path through the SCS's bridge type conditioner [35].

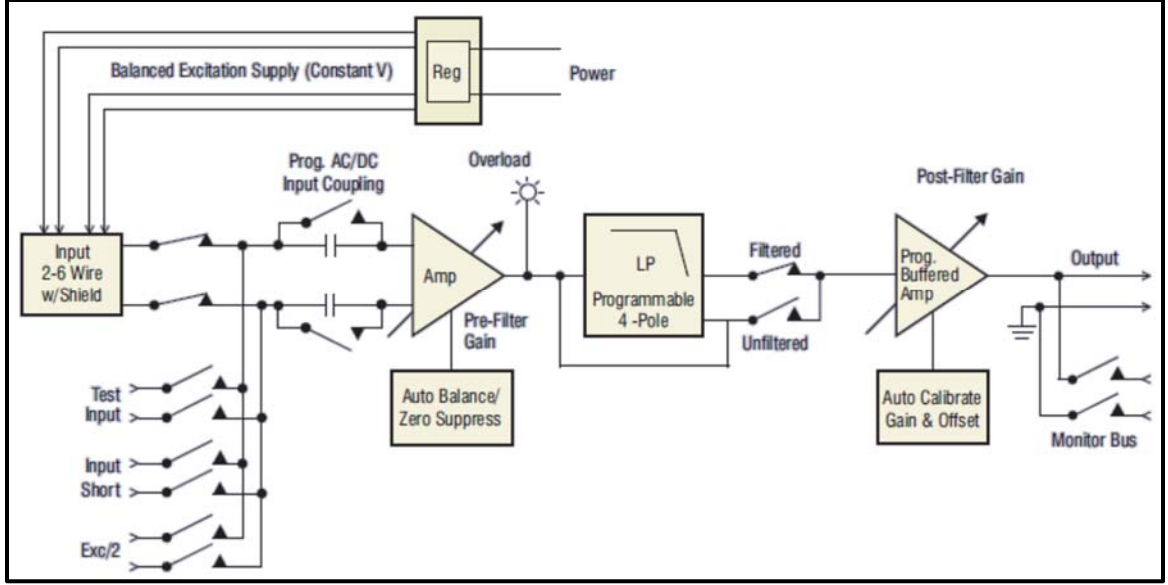


Figure 3.17 Simplified Bridge Type Conditioner Channel Block Diagram [35]

After consulting with the OEM [36], Table 3.7 lists the bridge conditioning parameters that contribute to bridge type measurement uncertainty.

The 95% confidence *t-distribution* coverage factor,  $c_{95\%}$ , for the normal distributions (random errors encountered when using the SCS) is 2, however, for the rectangular distributions (systematic errors encountered when using the SCS) the  $c_{95\%}$  is  $\sqrt{3}$  [34]. Manipulating Equation 2.14, the standard uncertainty is

$$u_r = \frac{U_{95\%}}{c_{95\%}} \quad (3.14)$$

The SCS equipment at this test area is housed in temperature controlled terminal rooms. As a result, the temperature is maintained at approximately 25°C. This negates all parameters dependent upon temperature drift in Table 3.7 since 25°C is the OEM's basis temperature for parameter evaluation. However, to assess the worst-case scenario



Table 3.7 Bridge Conditioner Uncertainty Parameters [35]

Parameter (P)	Value <sup>1</sup>	Unit	Distribution
1. Excitation Accuracy <sup>2</sup>	±0.1	%	Normal
2. Excitation Accuracy <sup>2</sup>	±5	mV	Normal
3. Excitation Temperature Drift <sup>3</sup>	±0.0025	%/°C	Rectangular
4. Excitation Temperature Drift <sup>3</sup>	±50	μV/°C	Rectangular
5. Auto Bridge Stability (of setting)	±0.0025	%/°C	Normal
6. Auto Bridge Drift	±1	μV/°C	Rectangular
7. Gain Error (of setting, maximum)	±0.2	%	Normal
8. Gain Temperature Coefficient	±0.005	%/°C	Normal
9. DC Linearity (of Full Scale [FS])	±0.01	% FS	Normal
10. Noise Referred-to-Input (RTI) <sup>4</sup>	6	μV RMS	Normal
11. Offset Drift RTI	3.5	μV/°C	Rectangular
12. Noise Referred-to-Output (RTO) <sup>4</sup>	100	μV RMS	Normal
13. Offset Drift RTO	150	μV/°C	Rectangular
14. Crosstalk	-80	dB	Normal
<sup>1</sup> OEM published values, see [35]. <sup>2</sup> Per OEM the excitation accuracy values must be summed. <sup>3</sup> Per OEM the excitation temperature drift values must be summed. <sup>4</sup> Per OEM a Crest Factor of 7 should be applied due to product qualification data.			

due to a temperature control failure in the terminal room, a separate evaluation will be conducted at the SCS's maximum operating temperature of 40°C. In light of these facts, the SCS standard uncertainty at 25°C for bridge conditioning is calculated as follows, (from Table 3.7)

$$u_{r,25^{\circ}C} = \sqrt{\left(\frac{U_{P1}}{t_m}\right)^2 + \left(\frac{U_{P2}}{t_m}\right)^2 + \left(\frac{U_{P7}}{t_m}\right)^2 + \left(\frac{U_{P9}}{t_m}\right)^2 + \left(\frac{U_{P10}}{t_m}\right)^2 + \left(\frac{U_{P12}}{t_m}\right)^2 + \left(\frac{U_{P14}}{t_m}\right)^2} \quad (3.15)$$

and at 40°C:

$$u_{r,40^{\circ}C} = \sqrt{\left(\frac{U_{P1}}{t_m}\right)^2 + \left(\frac{U_{P2}}{t_m}\right)^2 + \left(\frac{U_{P3}}{t_m}\right)^2 + \left(\frac{U_{P4}}{t_m}\right)^2 + \left(\frac{U_{P5}}{t_m}\right)^2 + \left(\frac{U_{P6}}{t_m}\right)^2 + \left(\frac{U_{P7}}{t_m}\right)^2 + \dots} \\ \sqrt{\left(\frac{U_{P8}}{t_m}\right)^2 + \left(\frac{U_{P9}}{t_m}\right)^2 + \left(\frac{U_{P10}}{t_m}\right)^2 + \left(\frac{U_{P11}}{t_m}\right)^2 + \left(\frac{U_{P12}}{t_m}\right)^2 + \left(\frac{U_{P13}}{t_m}\right)^2 + \left(\frac{U_{P14}}{t_m}\right)^2} \quad (3.16)$$

It should be noted that these uncertainty calculations are based on a maximum SCS input voltage of 10V; that parameters 1, 2, 3, 4, 7, 8, 9, 12, 13, and 14 are functions of the specific SCS channel gain; and the specific channel gain is calculated using the OEM's SCS internal channel gain calculator using [37]

$$Gain = \frac{FS_{out}}{(FS_{in})(Sensor_{sens})} \quad (3.17)$$

where  $FS_{out}$  is the excitation voltage,  $FS_{in}$  is the range of the load cell, and  $Sensor_{sens}$  is the sensitivity coefficient of the employed load cell. Additionally, parameters 2, 4, and 5 are functions of the SCS input voltage. The results of the SCS uncertainty analysis for typical tactical size rocket motor firing data is presented in Table 3.8

Table 3.8 SCS Uncertainty Analysis

Uncertainty Type <sup>1</sup>	25°C	40°C
Standard, $u_r$	$4.36 \times 10^{-5} V$	$5.90 \times 10^{-5} V$
Expanded, 95%, $U_r$	$8.73 \times 10^{-5} V$	$1.18 \times 10^{-4} V$
% at FS Voltage <sup>2</sup>	0.26%	0.35%
<sup>1</sup> Based on a channel gain of approximately 300. <sup>2</sup> Based on a maximum input voltage of 10V.		

#### D. Data Acquisition System (DAS)

The DAS employed for testing and experimentation at this test area is utilized only as a recording device, i.e., no internal attenuation or gain is applied, filtering is bypassed, and no unit conversion calculations are performed, see Figure 3.18.

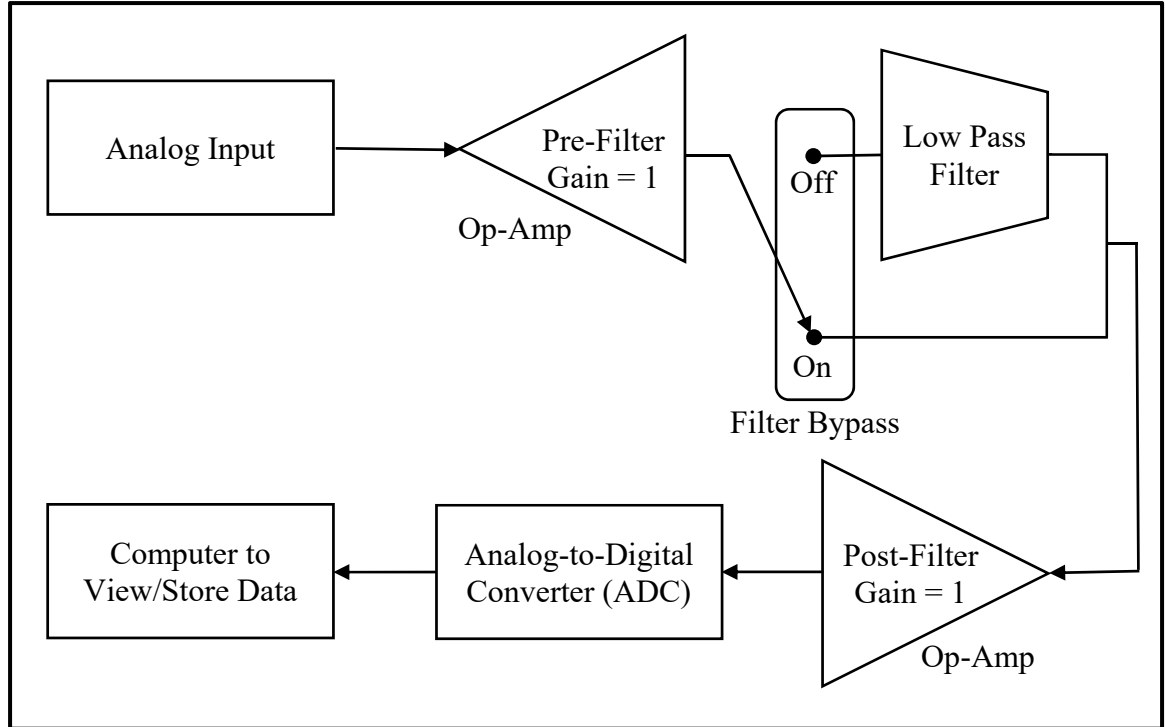


Figure 3.18 Simplified Schematic of Signal Path through the DAS

As a result, the 95% confidence voltage measurement expanded uncertainty is taken to be one-half the quotient of the maximum voltage range to the bit resolution of the ADC [20]

$$U_{ADC,95\%} = \frac{1}{2} \left( \frac{V_{max}}{2^n} \right) \quad (3.18)$$

where,  $V_{max}$  is the calibrated maximum voltage range and  $n$  is the number of ADC bits.

The full scale maximum voltage calibration range for these experiments was  $10V$  on a 16-bit DAS.

The DAS equipment at this test area is housed in temperature controlled control room. As a result, the temperature is maintained at approximately  $25^{\circ}C$ . Due to the other supporting electronics housed in this area, a loss of temperature control in the control room would suspend testing. This fact negates the need to consider any DAS uncertainty parameters dependent upon temperature drift. The DAS uncertainty analysis results are presented in Table 3.9.

Table 3.9 DAS Uncertainty Analysis

Uncertainty Type	$25^{\circ}C$
Standard, $u_r$	$3.8 \times 10^{-5} V$
Expanded, 95%, $U_r$	$7.63 \times 10^{-5} V$
% at FS Voltage <sup>1</sup>	0.00076%
<sup>1</sup> Based on an input voltage of $10V$	

#### E. Load Cell Calibration

Calibration, or the compensation required for a measured value to equal a known value, defines the accuracy of a measurement device and establishes traceability.

Calibration of load cells used for thrust measurements at this test area is typically performed at a local, independent 4:1 TUR calibration laboratory. This laboratory uses primary, NIST traceable deadweight force calibration machines which have been site compensated for local gravity and air buoyancy using [38]

$$Force = \frac{mg}{9.80665} \left( 1 - \frac{d}{D} \right) \quad (3.19)$$

where  $m$  is the mass of the weight,  $g$  is the local gravity (determined by site's local longitude, latitude, and elevation [39]),  $d$  is the local air density, and  $D$  is the density of the weight. These machines employ loading masses that are accurate to within two parts per million (PPM) or 0.00005% per pound, see Figure 3.19. For perspective, 0.00005% per pound is approximately the weight of a single, two-inch strand of average human hair [40].

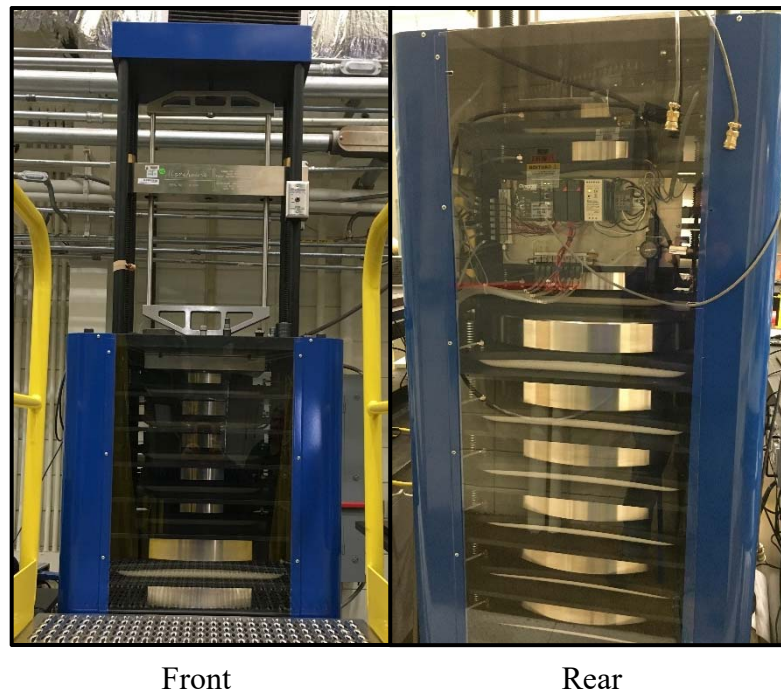


Figure 3.19 5,000 *lbf*, Primary Deadweight Force Calibration Machine

Following well established calibration guidance [41] the calibration laboratory exposes a load cell to three, 100% full scale load cycles at 0°, 120°, and 240° positions. From this procedure a host of calibration information is determined including, but not

limited to; ascending and descending polynomial coefficients, sensitivities, linearity, repeatability, and overall uncertainty. Table 3.10 presents the calibration laboratory results of overall uncertainty for the legacy load cell and the new design.

Table 3.10 Load Cell Calibration Uncertainty

Load Cell	Overall Uncertainty, 95% (%/FS)
Legacy	0.0029
New Design	0.0015

#### F. Overall Thrust Measurement Uncertainty

At this point the overall thrust measurement expanded uncertainty at 25°C for tactical size rocket motors static fired at this test area can be calculated using:

$$\%U_{overall,95\%} = \sqrt{(\%U_{cal}^2) + (\%U_{SCS}^2) + (\%U_{DAS}^2)} \quad (3.20)$$

The expanded uncertainty for a generic tactical rocket motor able to generate 5,000 lbf of thrust at this test area is presented in Table 3.11.

Table 3.11 Overall Thrust Measurement Uncertainty

Load Cell	Overall Uncertainty, 95% (% FS)	FS Thrust (lbf)	FS Thrust, 95% Confidence Interval (lbf) ± (lbf)
Legacy	0.26	5,000	5,000 ± 13
New Design	0.26	5,000	5,000 ± 13

## CHAPTER V

### CONCLUSIONS AND RECOMMENDATIONS

This work examined several sources of uncertainty for thrust measurements in a tactical-sized rocket static test stand. The sources examined included thrust oscillations from structural resonances, motor alignment, calibration procedures, and data acquisition. The results are based on experimental calibrations, alignment studies, and data from motor firings. The main design change examined was the design of a new load cell to address structural dynamics and measurement sensitivity to meet the uncertainty requirements.

The uncertainty analysis revealed that a 5,000 *lbf* thrust measurement can be made to within  $\pm 0.26\%$  of full scale with 95% confidence. The static test stand / motor structural resonance was identified as being the dominant driver influencing the quality of acquired thrust plots. It was shown that increasing the spring constant, or the stiffness, of the load cell shifted the resonance frequency from 422.06 *Hz* to approximately 1,761 *Hz*. This reduced the structural oscillations in the thrust measurement during motor firings, resulting from load cell resonance, to acceptable levels. With a new load cell in the measurement system, it was determined that the main source of thrust measurement uncertainty was due to errors introduced by the signal conditioning process, e.g., gain errors, departures from linearity, crosstalk, and electrical noise; calibration standards and digital storage uncertainties were deemed negligible in comparison. However, even the uncertainty of the signal conditioning, 0.26% of full scale at a 95% confidence, well exceeds this test area's target goal of one percent error for acquired thrust data.

Load cell stiffness and its effect on frequency response should not be understated and is a very important test design consideration in regards to the acquisition of clean and accurate thrust plots. A properly selected / designed load cell will virtually eliminate most requirements to digitally manipulate or post-process thrust data, e.g., filtering or data averaging, and prevent the unintentional suppression of any real-world physical phenomena. Also, correct load cell selection will alleviate the need to employ resonance suppressing hardware such as pre-load rigs or other dampening materials that negatively affect overall test event effectiveness and schedule.

The following is a list of recommendations generated by this research

- If possible, become familiar with the calibration laboratory and its procedures and processes. This will not only give the evaluator greater insight into what drives the calibration process but it will also build confidence and understanding the limits of the reported calibration data. Not to mention that building a good rapport with the laboratory personnel can pay dividends during those times when short suspense and speed are required.
- The largest measurement uncertainties at this test area originate from the signal conditioning equipment. It is imperative that the evaluator have a firm grasp on the end-to-end performance specifications of the employed signal conditioning equipment and understand the ramifications of the equipment's inherent errors.
- Thoroughly evaluate all alignment procedures and methods. This is especially important for test areas that may correct thrust data using pretest calibration curves.



- Properly select load cells based not only on maximum required loads but on its natural resonance frequency. Ensure the load cell's natural frequency, which is a function of the weight of the attached load, is above the frequency band of interest. This is a very important consideration for the generation of clean, true thrust data.

The following is a list of future endeavors related to this research.

- Replacing internal amplifier in the new design with an external amplifier to help reduce electrical noise propagation over long instrumentation line requirements.
- Explore addition of a torque measuring component in the new design enabling the evaluator to measure motor roll during static firings. This will also necessitate the use of spherical bearings in lieu of cylindrical bearing at the motor surface.
- Expand and apply this analysis methodology to large rocket motor testing at this test area.
- Investigate the automation of rocket motor centering and leveling, especially for large motors.
- Investigate the use of very low natural resonance frequency load cells, versus high natural frequency, that corresponds to the rise time of initial thrust. A load cell with a lower natural frequency may actually be a better choice since the primary interest is static in nature. There may be some low frequency ringing but most probably at a much lower level.

## Appendix A

### SCS Factory Acceptance Testing (FAT)

## SCS FAT Methodology

Instead of attempting to determine each internal error source of the SCS chassis electronics, a composite internal error based on a comparison of voltage in,  $V_{in}$ , versus voltage out,  $V_{out}$ , is utilized by the OEM. The composite internal error is determined using a calibrated Function / Waveform Generator (FWG) as the input signal to the SCS and a calibrated Digital Volt Meter (DVM) to measure the SCS output voltage. This output voltage is populated with all the internal errors imparted as a signal moves through the SCS. Consequently, all that is required to determine the overall SCS measurement uncertainty is the measurement uncertainty of the FWG and the DVM. Further, any FWG amplitude errors will also be captured in the  $V_{in}$  and  $V_{out}$  comparison. As a result, amplification, i.e., gain, measurement errors are used to define the overall composite internal error and uncertainty.

Gain errors,  $G_{err}$ , introduced by a non-inverting Operational Amplifier (Op-Amp), of the type used in the aforementioned SCS, are dependent upon the test frequency,

$$G_{err}(f) = \left( \frac{\left[ \frac{A_{OL\_DC}}{1 + \beta * A_{OL\_DC}} \right]}{\sqrt{\left[ 1 + \frac{f^2}{f_o^2} * \frac{1}{(1 + \beta * A_{OL\_DC})^2} \right]}} \right) \quad (A.1)$$

where  $A_{OL\_DC}$  is the Open-Loop (OL) gain at Direct Current (DC),  $f$  is the test frequency,  $f_o$  is the dominant pole of the Op-Amp, and

$$\beta = \frac{V_{fb}}{V_{out}} \quad (A.2)$$

where  $V_{fb}$  is the feedback voltage. Since gain errors are related to the test frequency and the Op-Amp's dominant filter pole, the relative filter error is determined by performing a gain error test with the filter on and with the filter bypassed. Differences in these gain error tests are then used to calculate the measurement variation due to the filter and, consequently, used to develop the overall SCS measurement uncertainty.

The gain error test, graphically illustrated in Figure A.1, can be performed in three steps:

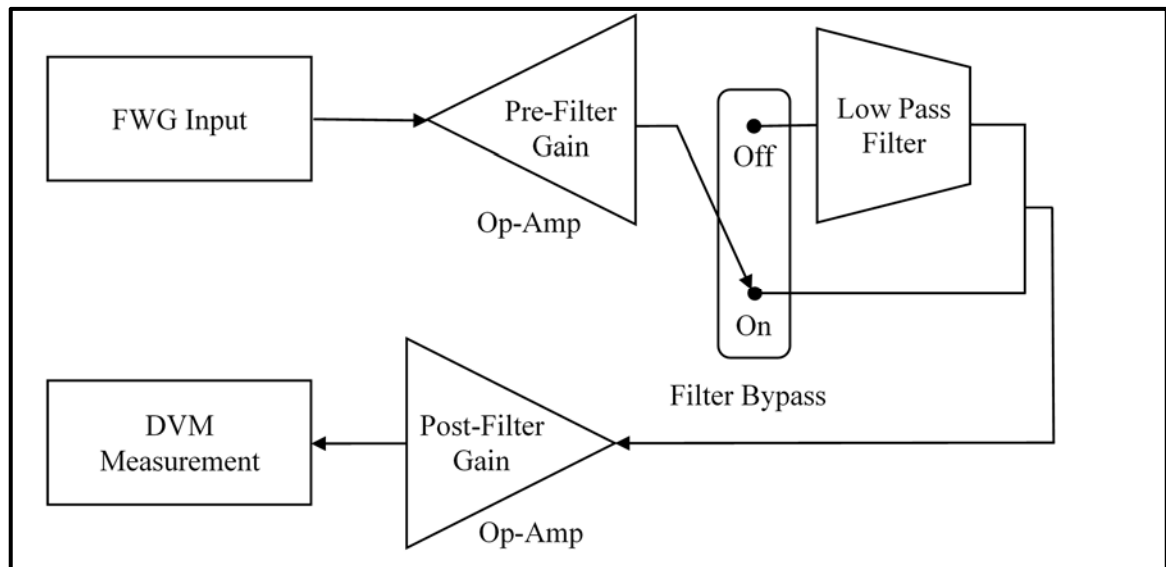


Figure A.1 Gain Error Test Method to Determine Overall SCS Uncertainty

- Step 1 - With the filter bypass on, apply a signal of known frequency and amplitude to the SCS input and record output,

- Step 2 - Without changing any other setting, turn the filter bypass off and apply the same signal (exact frequency and amplitude as in step one) to the SCS input and record output,
- Step 3 - Using the DVM's accuracy specifications calculate the uncertainty introduced by Step 1 and Step 2. Finally, these results are summed and used to calculate the overall SCS measurement uncertainty.

Per the OEM [36], there are two components that contribute to the DVM's error; noise and short term drift. When performing Alternating Current (AC) measurements, these errors are collectively termed Voltage Transfer Accuracy (for DC measurements the collective term is Transfer Accuracy). The OEM's DVM AC and DC characteristics are presented in Figure A.2 and A.3, respectively [42].

Accuracy Specifications ( % of reading + % of range )						
Function	Range	Frequency Range	24 Hour T <sub>CAL</sub> ± 1 °C	90 Day T <sub>CAL</sub> ± 5 °C	1 Year T <sub>CAL</sub> ± 5 °C	Temperature Coefficient 0 °C to (T <sub>CAL</sub> – 5 °C) (T <sub>CAL</sub> + 5 °C) to 55 °C
True RMS AC Voltage	100.0000 mV to 750.000 V	3 Hz – 5 Hz	0.50 + 0.02	0.50 + 0.03	0.50 + 0.03	0.010 + 0.003
		5 Hz – 10 Hz	0.10 + 0.02	0.10 + 0.03	0.10 + 0.03	0.008 + 0.003
	10 Hz – 20 kHz	0.02 + 0.02	0.05 + 0.03	0.06 + 0.03	0.005 + 0.003	
	20 kHz – 50 kHz	0.05 + 0.04	0.09 + 0.05	0.10 + 0.05	0.010 + 0.005	
	50 kHz – 100 kHz	0.20 + 0.08	0.30 + 0.08	0.40 + 0.08	0.020 + 0.008	
	100 kHz – 300 kHz	1.00 + 0.50	1.20 + 0.50	1.20 + 0.50	0.120 + 0.020	
Voltage Transfer Accuracy ( typical )						
Frequency	Error					
10 Hz to 300 kHz	(24 hour % of range + % of reading)/5					
Conditions:	<div>- Sinewave input only using slow filter.</div> <div>- Within 10 minutes and ±0.5 °C.</div> <div>- Within ±10% of initial voltage and ±1% of initial frequency.</div> <div>- Following a 2–hour warm–up.</div> <div>- Fixed range between 10% and 100% of full scale (and &lt;120 V).</div> <div>- Measurements are made using accepted metrology practices</div>					

Figure A.2 OEM Published DVM AC Characteristics [42]

Accuracy Specifications ( % of reading + % of range )						
Function	Range	Test Current or Burden Voltage	24 Hour $T_{CAL} \pm 1\text{ }^{\circ}\text{C}$	90 Day $T_{CAL} \pm 5\text{ }^{\circ}\text{C}$	1 Year $T_{CAL} \pm 5\text{ }^{\circ}\text{C}$	Temperature Coefficient 0 °C to ( $T_{CAL} - 5\text{ }^{\circ}\text{C}$ ) ( $T_{CAL} + 5\text{ }^{\circ}\text{C}$ ) to 55 °C
DC	100.0000 mV		0.0030+0.0030	0.0040+0.0035	0.0050+0.0035	0.0005+0.0005
	1.000000 V		0.0020+0.0006	0.0030+0.0007	0.0035+0.0007	0.0005+0.0001
	10.00000 V		0.0015+0.0004	0.0020+0.0005	0.0030+0.0005	0.0005+0.0001
	100.0000 V		0.0020+0.0006	0.0035+0.0006	0.0040+0.0006	0.0005+0.0001
	1000.000 V		0.0020+0.0006	0.0035+0.0006	0.0040+0.0006	0.0005+0.0001

**Transfer Accuracy (Typical)**

All DC volts, <0.12 A DC Current, < 1.2 MΩ: (24 hour % of range error) / 2)

All other DC current and resistance: (24 hour % of range error + % of reading)/2

Conditions:

- Within 10 minutes and  $\pm 0.5\text{ }^{\circ}\text{C}$
- Within  $\pm 10\%$  of initial value.
- Following a 2-hour warm-up.
- Fixed range.
- Using  $\geq 10$  NPLC.
- Measurements are made using accepted metrology practices.

Figure A.3 OEM Published DVM DC Characteristics [42]

Since the DVM is NIST traceable and calibrated on a yearly basis, worst-case errors are expected to manifest at or near the calibration anniversary date. With this in mind, use of the “1 Year” accuracy specification logically represents the most extreme errors at any given time within the DVM’s calibration cycle.

Pertinent FAT results are included within each signal conditioner’s specification sheet along with its specific characteristics. These values can then be used to calculate the signal conditioner’s measurement uncertainty and provide a level of confidence to the evaluator in regards to the viability and reliability of the calculated SCS measurement uncertainty.

## Appendix B

### Example Calculations

Load Cell Resonance Calculation						
Element	Full Load	Expended		Max	Max	
Weight	Weight	Weight		Load	Deflection	
(lbs)	(lbs)	(lbs)		(lbf)	(in)	
1.23	57	37		10000	0.0008	
	Prefire	Postfire				
me	ml	ml		k	g	
(lbs)	(lbs)	(lbs)		(lbf/in)	(in/s^2)	$\pi$
1.23	58.23	38.23		1.25E+07	386	3.141593
Unloaded Resonant Frequency =			9968.19	Hz		
Prefire Resonant Frequency =			1448.76	Hz		
Postfire Resonant Frequency =			1788.00	Hz		
Peak - Frequency Calculation						
Initial	Final					
Rise	Tail-off					
$\Delta t$	$\Delta t$					
(s)	(s)					
0.00323	0.00242					
Initial Rise Frequency =			309.60	Hz		
Final Tail-off Frequency =			413.22	Hz		



Sample	Pitch						
	14 inches between Fwd and Aft Measurement Locations)						
	Fwd	Fwd	Aft	Aft	Fwd-Aft	Slope	Angle
	(in)	$\Delta$ Baseline (in)	(in)	$\Delta$ Baseline (in)	$\Delta$ (in)		°
Baseline	9.6025		9.6		0.0025	1.79E-04	1.02E-02
1	9.6025	0	9.605	0.005	0.0025	1.79E-04	1.02E-02
2	9.6	0.0025	9.6075	0.0075	0.0075	5.36E-04	3.07E-02
3	9.6025	0	9.605	0.005	0.0025	1.79E-04	1.02E-02
4	9.5975	0.005	9.6	0	0.0025	1.79E-04	1.02E-02
5	9.6	0.0025	9.6025	0.0025	0.0025	1.79E-04	1.02E-02
6	9.6025	0	9.6075	0.0075	0.005	3.57E-04	2.05E-02
7	9.6025	0	9.6075	0.0075	0.005	3.57E-04	2.05E-02
8	9.605	0.0025	9.6075	0.0075	0.0025	1.79E-04	1.02E-02
9	9.6025	0	9.5975	0.0025	0.005	3.57E-04	2.05E-02
10	9.6025	0	9.6025	0.0025	0	0.00E+00	0.00E+00

DAS Uncertainty			
	Max		
# of bits	volts		
16	10		
Standard Uncertainty =		3.81E-05	volts
95% Uncertainty =		7.63E-05	volts
At Full-Scale Voltage =		0.00076	%

TBDG Uncertainty Measurement Calculations						
Analog Reading Uncertainty	=	2.89E-04				
Resolution Limit		0.0005				
Evaluator Uncertainty	=	1.28E-03				
Resolution Limit		0.0025				
Confidence Level		95%				
ICDF		1.959964				
Repeatability Uncertainty	=	6.72E-05				
Mean Sample Value		9.002125				
Standard Deviation		0.0002125				
Total TBDG Uncertainty (in)	=	1.31E-03				
Effective DOF TBDG Uncertainty	=	1.30E+06				
Since the degrees of freedom is greater than 31, the coverage factor = 2						
The uncertainty interval for this measurement = 2 for 95%						
Average deviation from the baseline = 9.002125 ± 0.002619033 inches						

Overall Thrust Measurement Uncertainty						
New Design	%Ucal	0.0015	%Uscs	0.26	%Udas	0.00076
Legacy	%Ucal	0.0029	%Uscs	0.26	%Udas	0.00076
		%U95%	New Design	0.260005	%FS	
			Legacy	0.260017	%FS	



## REFERENCES

- [1] Redstone Test Center, "Missile/Aviation Propulsion Testing," Redstone Test Center Test Capabilities [online database], [https://www.rtc.army.mil/Resources/Capability Sheets/Missile Aviation Propulsion Testing.pdf](https://www.rtc.army.mil/Resources/Capability%20Sheets/Missile%20Aviation%20Propulsion%20Testing.pdf) [retrieved 5 April 2017].
- [2] Anon., "Webster's II New College Dictionary," Houghton Mifflin Company, Boston, MA, 2001.
- [3] Tekscan, Inc., "Load Cell vs. Force Sensor," eBook [online book], <https://www.tekscan.com/resources/ebook/load-cell-vs-force-sensor> [retrieved 18 November 2015].
- [4] Copidate Technical Publicity, "How They Work," Strain Gauges [online tutorial], <http://www.sensorland.com/HowPage002.html> [retrieved 20 November 2015].
- [5] Zolotorev, N., Kuznetsov, V., and Konovalenko, A., "Optimization of the Stand for Test of Hybrid Rocket Engines of Solid Fuel," *MATEC Web of Conferences* 110, 01093, 2017.  
DOI: 10.1051/mateconf/201711001093
- [6] Peretz, A., Einav, O., Hashmonay, B.A., Birnholz, A., and Sobe, Z., "Development of a Laboratory-Scale System for Hybrid Rocket Motor Testing," *Journal of Propulsion and Power*, Vol. 27, No. 1, 2011, pp. 190-196.  
DOI: 10.2514/1.47521
- [7] Rugescu, R.D. and Sapunaru, R., "The Test Stand for ORVEAL Series of Combined Rocket Engines," *Applied Mechanics and Materials*, ISSN: 1662-7482, Vol. 436, 2013, pp. 10-17.  
DOI: 10.4028/www.scientific.net/AMM.436.10
- [8] Korting, P.A.O.G., Reitsma, H.J., "Theoretical and Experimental Evaluation of and Indoor Rocket Test Stand," *Journal of Spacecraft*, Vol 20, 1983, pp. 266-271.  
DOI: 10.2514/25591
- [9] Giligorijević, N., Živković, S., Subotić, S., Kozomara, S., Nikolić, M., and Čitaković, S., "Side Force Determination in the Rocket Motor Thrust Vector Control System," *Scientific Technical Review*, Vol. 63, No. 1, 2013, pp. 27-38.
- [10] Favato, L.F. and Magalhães, P.A.A., "Linear Static and Dynamic Analysis of Rocket Engine Testing Bench Structure using the Finite Element Method," *International Journal of Engineering Research and Applications*, ISSN: 2248-9622, Vol. 5, Issue 4 (Part – 7), 2015, pp. 70-77.

- [11] Knauber, R.N., "Thrust Misalignment for Fixed-Nozzle Solid Rocket Motors," *Journal of Spacecraft*, Vol 33, No. 6, 1996, pp. 794-799.  
DOI: 10.2514/3.26840
- [12] Gerards, A.B., "High Pressure Ballistic Evaluation Motor: The Development and Characterization of Army Ten-Pound Charge (ATPC) Motor," Master of Science Thesis, University of Alabama in Huntsville, Huntsville, AL, 2006.
- [13] Brimhall, Z.N., Atkinson, J.P., Kirk, D.R., and Peebles, H.G., "Design of Six Degree of Freedom Solid Rocket Motor Test Stand," *43<sup>rd</sup> Joint Propulsion Conference and Exhibit*, AIAA Paper 2007-5331, 2007.
- [14] Coppotelli, G. and Grappasonni, C., "Operational Modal Analysis of a Solid Rocket Motor from Firing Test," *Journal of Spacecraft and Rockets*, Vol. 50, No. 3, 2013, pp. 632-640.  
DOI: 10.2514/1.A32145
- [15] Renitha, P. and Sivaramapandian, J., "Design Analysis and Optimization of Thrust Measurement System for Testing Semi-Cryogenic Rocket Engine," *International Conference on Energy Efficient Technologies for Sustainability (ICEETS)*, 2016.  
DOI: 10.1109/ICEETS.2016.7583878
- [16] Kumar, A. and Anjaneyulu, L., "Emerging Trends in Instrumentation in Rocket Motor Testing Over Three Decades," *Defense Science Journal*, Vol. 65, No. 1, 2015, pp. 63-69.  
DOI: 10.14429/dsj.65.7949
- [17] Barber, B.C., "Thrust Measuring System for Electrothermal Thrusters," *Journal of Spacecraft*, Vol. 11, No. 8, 1974, pp. 449-554.  
DOI: 10.2514/3.62125
- [18] Xing, Q., Zhang, J., Qian, M., Zhenyuan, J., and Baoyuan, S., "Design and Optimization of a Piezoelectric Thrust-Measuring Platform for Attitude-Control Rocket Engines," *Applied Mechanics and Mathematics*, Vols. 44-47, 2011, pp. 1977-1981.  
DOI: 10.4208/www.scientific.net/AMM.44-47.1977
- [19] Sims, J.D. and Coleman, H.W., "Improving Hybrid Motor Thrust Measurements at Test Stand 500," *35<sup>th</sup> Joint Propulsion Conference and Exhibit*, AIAA Paper 99-2325, 1999.  
DOI: 10.2514/6.1999-2325
- [20] Coleman, H. W. and Steele, G.W., "Experimentation, Validation, and Uncertainty Analysis for Engineers Third Edition," John Wiley & Sons, Inc., Hoboken, NJ, 2009.
- [21] Taylor, J. L., "Computer-Based Data Acquisition Systems Design Techniques Second Edition," *Instrument Society of America*, Research Triangle Park, NC, 1990.

- [22] Meyn, L.A., "An Uncertainty Propagation Methodology that Simplifies Uncertainty," *38<sup>th</sup> Aerospace Sciences Meeting and Exhibit*, AIAA Paper 2000-0149, 1998.  
DOI: 10.2514/6.2000-0149
- [23] Smith, D.L., "Matrix Formalism for Uncertainty Analysis," *Review of Scientific Instruments* 54, 818, 1983.  
DOI: 10.1063/1.1137484
- [24] Chunfu, Z., Qijin, Y., and Jun, Z., "Application of Optimal Fitting in the Static Thrust Line Measurement of Solid Rocket Motor," *Applied Mechanics and Materials*, Vol. 128-126, 2012, pp. 1126-1130.  
DOI:10.4028/scientific.net/AMM.128-129.1126
- [25] Temple, G., Jize, N., and Wysocki, P., "Testability Modeling and Analysis of a Rocket Engine Test Stand," *IEEEAC*, Paper# 1127, Ver. 4, 2004.
- [26] Dauch, F.T., "Uncertainty Analysis of the Ultrasonic Technique Applied to Solid Propellant Burning Rate Measurement," Master of Science Thesis, University of Alabama in Huntsville, Huntsville, AL, 1999.
- [27] Sims, J.D., "Hysteresis Effects on Thrust Measurement and its Uncertainty," Master of Science Thesis, University of Alabama in Huntsville, Huntsville, AL, 2000.
- [28] Sims, J.D. and Coleman, H.W., "Hysteresis Effects on Thrust Measurement and its Uncertainty," *Journal of Propulsion and Power*, Vol. 19, No. 3, 2003, pp. 506-513.  
DOI: 10.2514/2.6135
- [29] Frederick, R.A. and Greiner, B.E., "Laboratory-Scale Hybrid Rocket Motor Uncertainty Analysis," *Journal of Propulsion and Power*, Vol. 12, No. 3, 1996, pp. 605-611.
- [30] Sims, J.D. and Coleman, H.W., "Results of a 24-inch Hybrid Motor Uncertainty Analysis," *34th Joint Propulsion Conference*, AIAA Paper 98-4021, 1998.  
DOI: 10.2514/6.1998-4021
- [31] Delta Metrics, Inc., Control Drawing and Data Sheet, Load Cell Model No. 99-3146-0001.
- [32] Delta Metrics, Inc., Control Drawing and Data Sheet, Load Cell Model No. 99-3583-010K.
- [33] Mitutoyo Corporation, "Double Column Height Dial Gauge," Operating Instructions.

- [34] Castrup, H., "Distributions for Uncertainty Analysis," *International Data Week (IDW) Conference*, 2001, Revised 2004.
- [35] Precision Filters, Inc., "Precision 28118 Octal-Channel Bridge Conditioner with Excitation Voltage," P8456 Rev D,  
[http://www.pfinc.com/library/pdf\\_files/current\\_product\\_specs/28118\\_spec\\_sheet.pdf](http://www.pfinc.com/library/pdf_files/current_product_specs/28118_spec_sheet.pdf)  
[retrieved 18 April 2017].
- [36] Firth, D., President, Precision Filters, Inc., Personal Interview, 2 November 2016.
- [37] Precision Filters, Inc., "28000 Test Subsystem, Operators Manual," Rev F, 2011.
- [38] Foster, K., Marshall Space Flight Center Metrology and Calibration Laboratory Manager, Personal Interview, 2 February 2016.
- [39] Fury, R. S., "National Geodetic Survey (NGS) Gravity Prediction Methodology, NOAA NGS Tools," 1999 [online], [https://www.ngs.noaa.gov/TOOLS/Gravity/grav\\_method.html](https://www.ngs.noaa.gov/TOOLS/Gravity/grav_method.html) [retrieved 5 May 2017].
- [40] Legrand, M., Passos, C.J.S., Mergler, D., and Chan, H.M., "Biomonitoring of Mercury Exposure with Single Human Hair Strand," *Environmental Science & Technology*, Vol. 39, No. 12, 2005, pp. 4594-4598.
- [41] ASTM E74-13a, "Standard Practice of Calibration of Force-Measuring Instruments for Verifying the force Indication of Testing Machines," 2013.  
DOI: 10.1520/E0074-13A
- [42] Agilent Technologies, Inc., "Agilent 34410A/11A 6½ Digit Multimeter, Service Guide," Fourth Edition, Part No. 34410-90010, 2007.
- [43] Thomas, J. C., Stahl, J. M., Morrow, G. R., and Petersen, E. L., "Design and Characterization of a Lab-Scale Hybrid Rocket Test Stand," *52nd AIAA/SAE/ASEE Joint Propulsion Conference*, AIAA Paper 2016-4965, 2016.  
DOI: 10.2514/6.2016-4965
- [44] Runyan, R. B., Deken, L. R., and Miller, T. J., "Structural Dynamics of a Small Rocket Thrust Stand," *28th AIAA/SAE/ASEE Joint Propulsion Conference and Exhibit*, AIAA Paper 92-3787, 1992.  
DOI: 10.2514/6.1992-3787
- [45] Arrington, L. A., and Schneider, S. J., "Low Thrust Rocket Test Facility," *26th AIAA/SAE/ASEE Joint Propulsion Conference*, AIAA Paper 90-2503, 1990.  
DOI: 10.2514/6.1990-2503

- [46] Stevenson, T. and Lightsey, G., “Design and Operation of a Thrust Test Stand for University Small Satellite Thrusters,” *AIAA Aerospace Sciences Meeting*, AIAA Paper 2018-2117, 2018.  
DOI: 10.2514/6.2018-2117
- [47] Langill, A. W. and Kapandritis, G. N., “Multi-Component Test Fixtures for Solid Rocket Motor Testing,” *IEEE Transactions on Aerospace-Support Conference Procedures*.
- [48] Hill, C., Doerksen, G., Stannard, D., Hinman, W. S., Quinn, D., and Johansen, C., “Development and Testing of a 4.4-kN Paraffin-based Hybrid Rocket Motor and Test Facility,” *2018 Joint Propulsion Conference*, AIAA Paper 2018-4837, 2018.  
DOI: 10.2514/6.2018-4837
- [49] Dunn, Z., Dyery, J., Lohnery, K., Doran, E., Bayart, C., Sadhwani, A., Zilliac, G., Karabeyoglu, A., and Cantwell, B., “Test Facility Development for the 15,000 lb Thrust Peregrine Hybrid Sounding Rocket,” *43rd AIAA/ASME/SAE/ASEE Joint Propulsion Conference and Exhibit*, AIAA Paper 2007-5358, 2007.  
DOI: 10.2514/6.2007-5358
- [50] Spurling, J., Bustamante, R., Kim, S., Sarigul-Klijn, N., and McGuire, N., “Design and Development of a Vertical Test Stand for Hybrid Propulsion Acoustic Signature Measurements,” *42nd AIAA/ASME/SAE/ASEE Joint Propulsion Conference and Exhibit*, AIAA Paper 2006-4409, 2006.  
DOI: 10.2514/6.2006-4409